



**HAL**  
open science

## The Dinaric fault system: Large-scale structure, rates of slip, and Plio-Pleistocene evolution of the transpressive northeastern boundary of the Adria microplate

Adrien Moulin, Lucilla Benedetti, Magali Rizza, Petra Jamšek Rupnik, Andrej Gosar, Didier Bourles, Karim Keddadouche, Georges Aumaitre, Maurice Arnold, Valery Guillou, et al.

### ► To cite this version:

Adrien Moulin, Lucilla Benedetti, Magali Rizza, Petra Jamšek Rupnik, Andrej Gosar, et al.. The Dinaric fault system: Large-scale structure, rates of slip, and Plio-Pleistocene evolution of the transpressive northeastern boundary of the Adria microplate. *Tectonics*, 2016, 35, pp.2258 - 2292. 10.1002/2016TC004188 . hal-01420780

**HAL Id: hal-01420780**

**<https://amu.hal.science/hal-01420780>**

Submitted on 21 Dec 2016

**HAL** is a multi-disciplinary open access archive for the deposit and dissemination of scientific research documents, whether they are published or not. The documents may come from teaching and research institutions in France or abroad, or from public or private research centers.

L'archive ouverte pluridisciplinaire **HAL**, est destinée au dépôt et à la diffusion de documents scientifiques de niveau recherche, publiés ou non, émanant des établissements d'enseignement et de recherche français ou étrangers, des laboratoires publics ou privés.



## Tectonics

### RESEARCH ARTICLE

10.1002/2016TC004188

#### Key Points:

- Pleistocene slip rates of the Dinaric faults are derived from displaced markers and  $^{36}\text{Cl}$  CRE ages
- Chronological bounds are placed on the kinematic evolution of the Dinarides over the Plio-Pleistocene
- Deformation in the Dinarides absorbs most of the Adria microplate rotation (versus stable Eurasia)

#### Supporting Information:

- Supporting Information S1
- Table S1

#### Correspondence to:

A. Moulin,  
moulin@cerege.fr

#### Citation:

Moulin, A., et al. (2016), The Dinaric fault system: Large-scale structure, rates of slip, and Plio-Pleistocene evolution of the transpressive northeastern boundary of the Adria microplate, *Tectonics*, 35, 2258–2292 doi:10.1002/2016TC004188.

Received 22 APR 2016

Accepted 30 AUG 2016

Accepted article online 7 SEP 2016

Published online 6 OCT 2016

## The Dinaric fault system: Large-scale structure, rates of slip, and Plio-Pleistocene evolution of the transpressive northeastern boundary of the Adria microplate

Adrien Moulin<sup>1</sup>, Lucilla Benedetti<sup>1</sup>, Magali Rizza<sup>1</sup>, Petra Jamšek Rupnik<sup>2</sup>, Andrej Gosar<sup>3</sup>, Didier Bourlès<sup>1</sup>, Karim Keddadouche<sup>1</sup>, Georges Aumaître<sup>1</sup>, Maurice Arnold<sup>1</sup>, Valéry Guillou<sup>1</sup>, and Jean-François Ritz<sup>4</sup>

<sup>1</sup>Aix-Marseille Université, CEREGE CNRS-IRD UMR 34, Aix-en-Provence, France, <sup>2</sup>Geological Survey of Slovenia, Ljubljana, Slovenia, <sup>3</sup>Seismology and Geology Office, Slovenian Environment Agency, Ljubljana, Slovenia, <sup>4</sup>Laboratoire Geosciences-UMR CNRS 5243, Université Montpellier 2, Montpellier, France

**Abstract** Located at the northeastern corner of the Adria microplate, the Alps-Dinarides junction represents a key region for understanding how the Adria microplate interacts with stable Europe. However, little is known on how the present-day deformation imposed by the rotation of the Adria microplate is absorbed across the Dinarides. Using morphotectonic analysis based on satellite and aerial images, accurate topographical maps, and digital elevation models combined with field investigations, we mapped in detail the three main active faults of the Northern Dinarides. Geomorphic and geological cumulative displacements ranging from a few meters to several kilometers have been identified on those faults and dated for the most recent ones using  $^{36}\text{Cl}$  exposure dating. Those results yielded a total right-lateral motion of  $3.8 \pm 0.7$  mm/yr oriented N317. Comparing our results with the motion expected from Adria rotation models suggests that the Northern Dinarides absorbs most of the predicted Adria-Eurasia motion, thus representing the eastern boundary of the microplate. However, a significant E-W component is lacking, suggesting that part of the stress imposed by the microplate rotation is transferred farther to the east. Finally, bounds placed on the Plio-Pleistocene kinematics confirm that faulting onset occurred during the Early Pliocene and evidence a significant kinematic change at the Early/Middle Pleistocene boundary.

### 1. Introduction

The convergence between Nubia and Eurasia causes active deformation across the Mediterranean [e.g., McKenzie, 1972; Anderson and Jackson, 1987; Westaway, 1990; Nocquet and Calais, 2004]. In the central Mediterranean, the Adriatic region is relatively aseismic, circumscribed by the Apennines, the Southern Alps, and the Dinarides [Anderson and Jackson, 1987; McKenzie, 1972]. Evidence from seismological, geodetic, and geological studies all suggest that this region moves independently of the two major plates, which defines the Adria microplate that rotates counterclockwise around a pole located in the Western Alps or in the western part of the Po plain [Calais et al., 2002; Ward, 1994; Westaway, 1990; Weber et al., 2010]. While the observed active deformation agrees with the slip vectors predicted by the models across the Apennines (ENE-WSW extension [Anzidei et al., 2001; Chiaraluce et al., 2004; D'Agostino et al., 2001; Piccardi et al., 1999; Schlagenhauf et al., 2011]) and Southern Alps (N-S shortening [Benedetti et al., 2000; D'Agostino et al., 2005; Grenczy et al., 2005; Weber et al., 2010]), it is unclear how Adria interacts with Eurasia along its eastern boundary. Along the Dinaric Belt, which follows the eastern Adria boundary, earthquake focal mechanisms ( $M \geq 4.5$  since 1963) indicate that strike-slip deformation plays a major role in accommodating the Adria motion across its NE rim (Figure 1; see also Herak et al. [1995] and Pondrelli et al. [2006] for the southwestern section of the Dinarides), which is in contrast with the pure convergence predicted by models [e.g., Nocquet, 2012].

The northern stretch of the Dinarides starts from the eastern tip of the E-W oriented Southern Alps, where the 1976 Friuli seismic sequence nucleated ( $M_w =$  up to 6.5, with thrust focal mechanisms) and runs southeastward for at least 100 km (Figure 1). Strike-slip focal mechanisms also match the motion along the NW-SE oriented right-lateral strike-slip faults called the Dinaric faults [Vrabec and Fodor, 2006]. For example, two moderate-sized earthquakes ruptured the Ravne Fault in 1998 and 2004 ( $M_w = 5.6$  and 5.2, respectively) [Kastelic et al., 2008] at the junction between the Southern Alps and the Northern Dinarides, and two small-sized earthquakes occurred to the SE along the Raša Fault in 1995 and 2013 ( $M_w = 4.7$  and 4.6, respectively). Based on

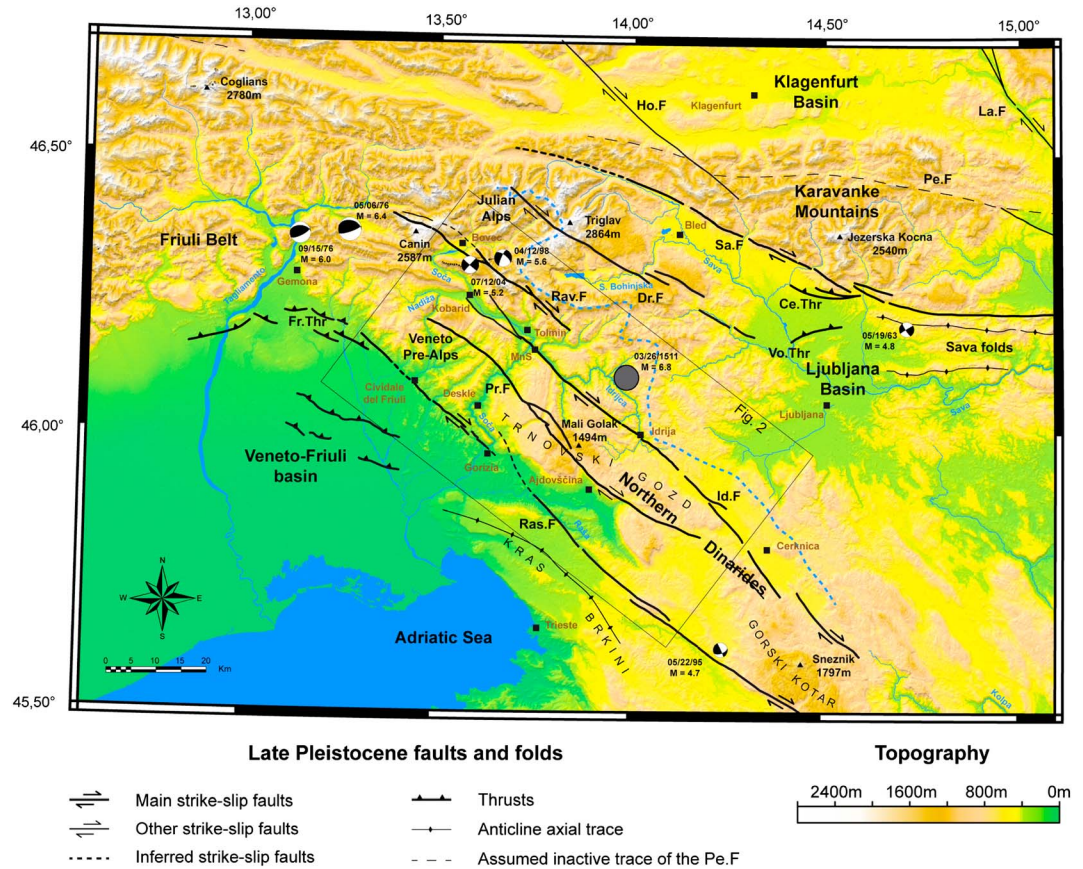


**Figure 1.** Seismotectonic map at the transition between the Southern Alps (represented here by the Friuli Belt, the Julian Alps, and the Karavanke Mountains) and the Northern Dinarides, showing the main active faults mapped from 2.5 m SPOT images, topographic maps, and illuminated DEMs. The focal mechanisms of earthquakes with magnitudes  $>4.5$  are also shown (only the two main shock waves of the 1976 Friuli seismic crisis are represented). The probable epicenter of the 1511 Idrija earthquake is represented in grey [Camassi *et al.*, 2011; Ribarič, 1979]. The blue dashed line represents the Adriatic Sea/Black Sea water divide. Pe. F = Periadriatic Fault; Ho. F = Hochtstuhl Fault; La. F = Labot Fault; Fr. Thr = Friuli thrusts; Rav. F = Ravne Fault; Dr. F = Dražgoše Fault; Sa. F = Sava Fault; Ce. Thr = Cerklje thrust; Vo. Thr = Vodice thrust; Id. F = Idrija Fault; Pr. F = Predjama Fault; and Ras. F = Raša Fault (Pe. F, Ho. F, and La. F are from Vrabc *et al.* [2006] and Sa. F, Ce. Thr, and Vo. Thr from Jamšek-Rupnik [2013]; other active faults have been mapped from our observations).

macroseismic data analysis, the 1511 Idrija earthquake ( $M_L = 6.8$ ), the largest event recorded in the area, occurred along a NW-SE oriented fault, likely in the central section of the Idrija Fault [Bavec *et al.*, 2012; Bavec *et al.*, 2013; Fitzko *et al.*, 2005; Ribarič, 1979] (Figure 1). Finally, Caporali *et al.* [2013] also suggest that right-lateral transpressive motion is required along the Northern Dinarides to generate a geodetic velocity field (data from 1999 to 2010 collected by permanent GPS stations positioned across the eastern Alps and the Northern Dinarides).

The purpose of this paper is to constrain the recent (late Pleistocene-Holocene) displacement vector across the Northern Dinarides and discuss how deformation is accommodated in this region as a result of Adria rotation. Kastelic *et al.* [2008] mapped the section of the Ravne Fault that ruptured during the 1998 and 2004 earthquakes. Moreover, clear evidence of recent motion has been recognized from airborne lidar topographic data along the central part of the Idrija Fault, enabling detailed mapping of the active fault trace [Cunningham *et al.*, 2006; Moulin *et al.*, 2014] and a first quantitative slip rate estimate of between 1 and 4 mm/yr that varies with time [Moulin *et al.*, 2014]. Further evidence of active faulting in the Northern Dinarides, however, remains insufficient for achieving the intended purpose.

Here we provide new data that allow identifying the shallow trace of the active faults in this area, characterizing their kinematics and discussing the relationships between the current on-fault motion, the seismicity, and the deeper structures. Due to the absence of deformed units younger than Eocene (Figure 2a), to identify

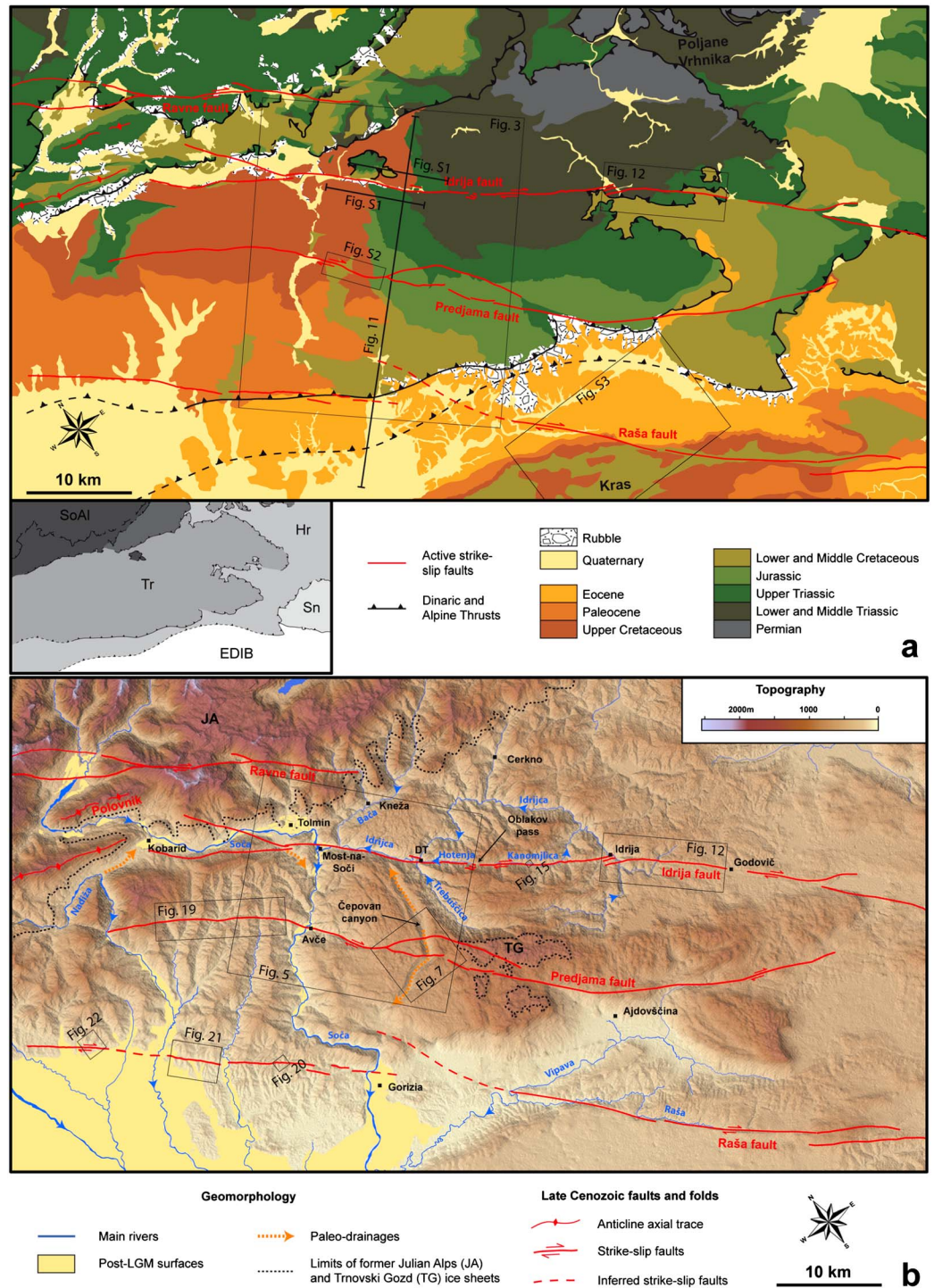


**Figure 2.** (a) Simplified geological map of the studied area (modified from *Buser et al.* [1967], *Buser* [1968], and *Buser et al.* [1986]) showing the main stratigraphic units. Thrusts related to the Eocene-Oligocene and Miocene compression phases are represented with black lines, and active fault traces are represented with red lines. The black box labeled Fig. S2 roughly identifies the extent of the two cross sections presented in supporting information Text S1. The inset at the left shows a sketch map of the main structural units of the Eocene-Oligocene and Miocene phases according to *Placer et al.* [2010] (SOAI = Southern Alps; Tr = Trnovo nappe; Hr = Hrušica nappe; Sn = Snežnik thrust block; and EDIB = External Dinaric Imbricated Belt). (b) Geomorphological map based on the 12.5 m DEM of the studied area showing the main drainage features (active rivers, main abandoned drainages, and postglacial surfaces modified from *Fontana et al.* [2008]). The maximum extent of the LGM ice sheets is represented by black dotted lines (JA = Julian Alps ice sheet; TG = Trnovski Gozd ice sheet; DT = Dolenja Trebuša). Active fault traces are represented in red.

the most recent displacements along the Dinaric faults, we studied the geomorphic expression of the Dinaric faults while searching for landforms that exhibit surface offsets along the strike of the faults. We used SPOT images, 12.5 and 5 m resolution digital elevation models (DEMs) (in the Slovenian and Italian territories, respectively), and 1/25,000 scale topographic maps to characterize the fault traces and identify morphological markers suitable for quantifying cumulative displacements that ranged from a few meters to several kilometers. The smallest offsets were constrained using a 1 m lidar DEM (first presented in *Moulin et al.* [2014]), local kinematic GPS surveys, 50 cm resolution orthophotos, and a 5 m resolution DEM derived from 1:5000 scale topographical maps. In addition, we tested the use of cosmogenic  $^{36}\text{Cl}$  in exhumed bedrock, buried bedrock, and on conglomerates capped by 30–40 cm thick soils to determine the ages of the offset fluvial markers. These analyses, combined with the geological data, were used to assess the recent slip rates of the Idrija, Predjama, and Raša Faults and to place kinematical bounds on the faulting history.

## 2. Large-Scale Morphology and Fault Geometry

### 2.1. Relief and Inherited Morphology

The northern part of the Dinarides, studied in the present article, is a NW-SE oriented belt that extends from the Julian Alps to Mt. Sneznik in the SE (Figure 1), separating the southward sloping Veneto-Friuli Plain in the west (elevations from 150 m above sea level (asl) to the present sea level) from the southeastward sloping Ljubljana Basin (mean elevation of 350 m asl) in the east. For convenience, this section of the Dinaric fold-thrust belt will be referred to as the “Northern Dinarides” in the following.

The Adriatic Sea/Black Sea water divide (dashed blue line in Figure 1) roughly follows the eastern edge of the Northern Dinarides, parallel to the Idrija Fault trace (Figure 1). In the northern part, at the junction with the Southern and Julian Alps, glaciers were most probably covering the most prominent reliefs during Last Glacial Maximum (LGM) [e.g., *Bavec et al.*, 2004; *Fontana et al.*, 2008; *Monegato et al.*, 2007]. South of the former Alpine icecap and because of a relatively low mean elevation and the influence of the Mediterranean climate, glacial deposits are exposed only in a small area (referred to as “TG” in Figure 2b) surrounding the 1494 m maximum elevation of the Mali Golak (Figure 1), and the morphology has been substantially affected by karstic processes. Different levels of karst tableland with a mean elevation of approximately 800 m (the Trnovski Gozd, Kras, Brkini, and Gorski Kotar areas characterized by abundant dolines and poljes) are visible along the belt (Figures 1 and 2b).

### 2.2. Fault Geometry

The 150 km long NW-SE oriented Dinaric fault system (DFS), encompassing the main active faults of this area, stretches between 46.3°N and approximately 45.2°N along a N315 mean direction (Figure 1). At its northwestern tip, the DFS interferes in the west with the E-W oriented active thrusts of the Friuli Belt [*Aoudia et al.*, 2000], while in the ENE, right-lateral strike-slip faults (Ravne, Dražgoše, and Sava Faults) of similar NW-SE-orientation but shorter lengths are observed from the Julian Alps to the Karavanke Mountains [*Jamšek Rupnik et al.*, 2012; *Jamšek-Rupnik*, 2013]. Toward the SE, the DFS extends at least up to the Mt. Sneznik in Croatia (Figure 1). In the study area from the NE to the SW, the DFS is composed of three main subparallel right-lateral strike-slip faults: the Idrija, Predjama, and Raša Faults, which are separated from one another by 10 to 15 km. Striking roughly parallel to the general N310–N315 trend of the Dinaric Belt, these faults are mainly intramountain faults, composed of 10–18 km long segment, except the northwestern section of the Raša Fault, which is located at the mountain front facing the Veneto-Friuli Plain (Figures 1 and 2).

The Predjama Fault also starts 10 km south of Godovič and appears as a branch of the relatively linear and steeply NE dipping [Čar, 2010; *Moulin et al.*, 2014; *Poljak et al.*, 2000] Idrija Fault (Figures 1 and 2). At 5 km east of Ajdovščina, the Predjama Fault splits into two branches along with a bend in the fault strike (Figure 2b). Overall, the Idrija and Predjama faults tend to parallel one another (Figure 2b), suggesting that these faults could merge at depth. The Raša Fault is more linear, cuts into the Kras plateau in the SE, and then continues along the range front NW of Gorizia (Figures 1 and 2b), separating the incised valleys grading down from the Veneto Prealps from the Veneto-Friuli Plain composed of Plio-Quaternary deposits (Figures 1 and 2).

Between Trieste and Gorizia, a 15 km wide fold runs parallel to and SW of the Raša Fault and forms the core of the Kras plateau. It exhibits evidence of Pleistocene activity, such as an abandoned and perched valley, which appears in green tones on the DEM (10–15 km SSW of Gorizia; Figure 1) and lies orthogonal to the anticline

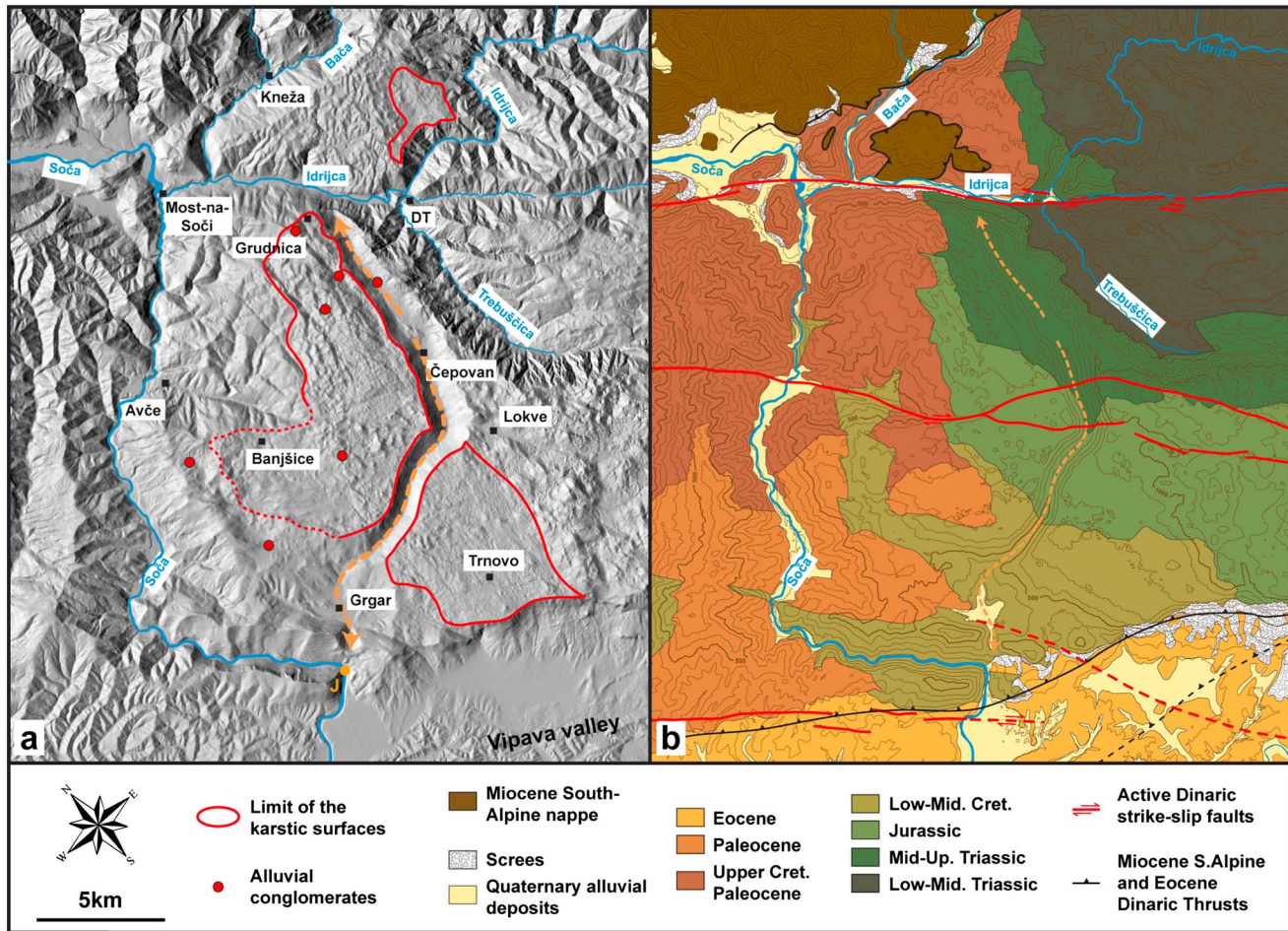


**Figure 3.** (a) Shaded 12.5 m DEM of the Trnovski Gozd plateau. Observations and inferences from *Habič* [1968] are reported. Red points represent perched fluvial sediments, red lines are the limits of the former alluvial plain that was subsequently karstified, and the orange dashed line represents the former drainage in the Čepovan Canyon. The orange solid line represents the possible extent of the karstified alluvial plain in the NE based on geological and morphological comparisons with the extent inferred by *Habič* [1968]. Point J corresponds to the former junction between the Soča River and the Čepovan Canyon. (b) Geological map of the Trnovski Gozd plateau and active faults in red. Note that karstified areas are mainly located where Middle-Upper Triassic to Middle Cretaceous limestones crop out. The elevation represented by the contour lines is 100 m.

axis. Although this structure probably plays an important role in accommodating the recent deformation, it is not included in the present study.

### 3. Quantitative Assessments of Long-Term Faulting and Folding Inferred From the Geometries of Large Drainages and the Čepovan Canyon

In this section, we focus on the Trnovski Gozd area (Figures 2 to 4), which is located at the junction between the upper Soča catchment in the north and the pure karst regions in the SE, to detect long-term displacements along the Idrija and Raša Faults and then investigate vertical displacements across the DFS.

#### 3.1. The Trnovski Gozd Plateau and Čepovan Paleocanyon

In this area, three main rivers converge near Most-na-Soči: the Bača and Soča Rivers, originating in the Julian Alps, and the Idrija River, flowing from the Northern Dinarides in the SE. The largest drainages of the Idrija watershed (Idrija, Hotenja, Kanomljica, and Trebušnica Rivers) are confined along deep and narrow valleys mostly oriented parallel to the NW-SE-striking Dinaric faults, which suggests tectonic control of the current drainage geometry (Figures 1 and 2). All these NW-SE-trending valleys have incised into the Mesozoic rocks of the Trnovski Gozd plateau, and the amount of incision has reached approximately 500 m along the largest

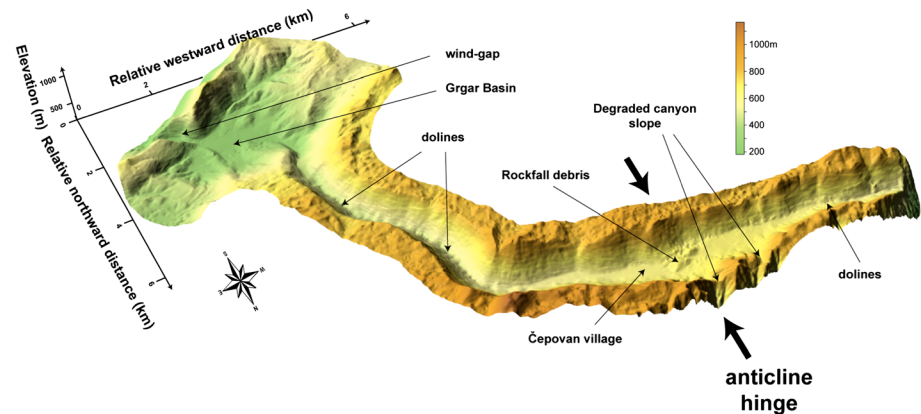


**Figure 4.** A 3-D view of the Čepovan Canyon looking WSW and showing the main geomorphic features along the canyon.

ivers. SW-to-W dipping Upper Triassic to Lower Cretaceous limestones and dolomites in some places on the plateau have controlled the development of a regular and karstified surface that composes the bulk of the plateau (area encircled in red in Figure 3a) [Habič, 1968, 1997]. Where the lithology changes from Mesozoic limestones and dolomites into Eocene flyschs, the drainage of karst area turns into poorly incised temporary drainages.

The fan shape drawn by this karstic surface contains fluvial sand and gravel sediments at the surface in the form of (1) remnants of karstified terraces along a N-S oriented tongue extending for 9 km south of Grudnica and (2) isolated patches located 3–4 km SE, WNW, and SW to Banjšice and up to the southwestern rim of the plateau near Trnovo [Habič, 1968, 1997] (Figure 3a). These sedimentary remains were used to infer the presence of a wide gravel-covered plain, which formerly drained water toward the SW and was subsequently abandoned and karstified when the current active drainages deepened [Habič, 1968].

Carved in the karst surface of the Trnovski Gozd plateau, the 15 km long Čepovan dry canyon, which is punctured by 20–60 m deep dolines, forms a consistent 1.1–1.6 km wide, 300 m deep V-shaped valley with steep sides ( $\sim 50^\circ$ ) (Figures 2b, 3, and 4). Additionally, the presence of fluvial deposits along the northernmost section of the canyon suggests that water previously flowed through the canyon [Habič, 1968] (Figure 3). Moreover, the hypothesis that the Čepovan Valley is of glacial origin can be ruled out since the reconstructed maximum extent of the Trnovski Gozd ice sheet is clearly higher [Habič, 1997] (Figure 2b). Based on these observations, Habič [1968] suggested that the Čepovan Canyon resulted from downcutting by a SW flowing river. Thus, the abandonment and karstification of the former alluvial plain would have been controlled by the onset of incision along the active drainages and the Čepovan Canyon. This widespread deepening of valleys is assumed to have occurred during the Plio-Pleistocene climatic transition [Habič, 1968].

In the SW, the Čepovan Canyon ends in the Grgar karstic depression, itself bounded by a NW-SE oriented ridge (Figures 3 and 4). The 300 m deep, 1 km wide, V-shaped wind gap observed across this ridge (Figures 3 and 4) probably represents the continuation of the Čepovan Canyon (Figure 3). We thus interpret the Čepovan Canyon to be a former fluvial drainage that has been subsequently abandoned and perched at about 350 m above the actual bottom of the Idrija Valley in the north and 250 m above the Soča in the SW (Figure 4).

### 3.2. Kilometric Displacement Along the Idrija Fault

The main valleys in Figure 4 (Soča, Bača, and Idrija) are all carved into the Trnovski Gozd plateau and display similar morphologies, with a mean width of 1.5 km and incision depths of approximately 500–600 m. The 3.7 km long  $0.56^\circ$  southward sloping Čiginj Valley 2–3 km SW of Tolmin is also comparable in size and is separated from the Soča Valley by the Bučenica and Mrzli hills in the SE (Figure 5a). The Čiginj Valley is presently drained by the Ušnica Creek, which is extremely small compared to the dimensions of the valley. This mismatch in size suggests that the valley was probably shaped by a far greater drainage and therefore might also be an abandoned valley.

As shown in Figures 2 and 3, the main Idrija Fault trace was derived from *Moulin et al.* [2014] and follows a path similar to the geological fault trace [Buser et al., 1986]. Figure 5a shows that the active drainages draw

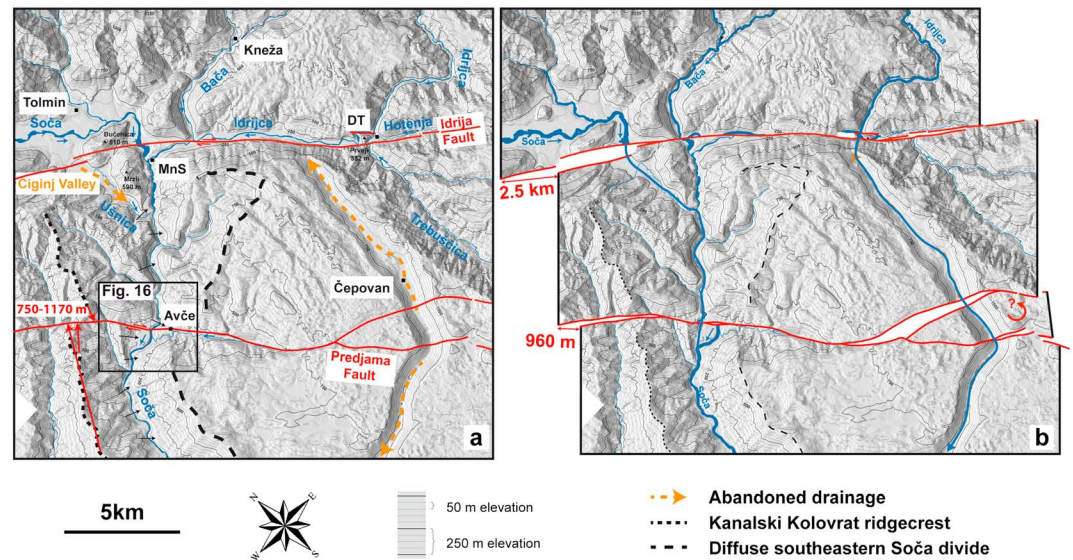


**Figure 5.** (a) Shaded 12.5 m DEM of the area between the Soča River and the Čepovan Canyon and across the Idrinja and Predjama Faults (in the NW, only the major branch of the Idrinja Fault is represented for simplification), showing the main drainage features. Black arrows show the alluvial terraces preserved along the Soča River. Red arrows NW of Avče represent the piercing lines used to measure tectonic displacements. MnS = Most-na-Soči; DT = Dolenja Trebuša. (b) The 2.5 km and 960 m back-slipping along the Idrinja and Predjama Faults, respectively, showing restored continuity of the main drainage features: the Soča with the Čiginj Valley, the Bača with the Soča, and the Idrinja with the Čepovan Canyon from NW to SE. The circling arrow indicates possible rotation of the fault-bounded block in the middle of the Čepovan Canyon.

a peculiar geometry across the Idrinja Fault. In the NE the Soča, Bača, and Idrinja Rivers tend to intersect the fault at a high angle. Those three rivers then converge along the fault into the Soča River near Most-na-Soči, which flows again with a perpendicular orientation in the SW. The two abandoned valleys observed in the area (Čepovan and Čiginj) are located in the SW and tend to also intersect the Idrinja Fault at a high angle. As a consequence, the general geometry displays an obvious northwestward shift in the active and abandoned valleys SW of the fault with respect to the valleys in the NE, what could be interpreted as a long-term right-lateral offset along the Idrinja Fault. Back-slipping the entire fault section by 2.5 km restores the continuity of the valleys on both sides of the fault and suggests that the Čiginj and Čepovan valleys formerly used to drain the Soča and Idrinja Rivers, respectively (Figure 5b). For the Idrinja and Bača Rivers, the realigned valley sections are linear and drain deeply entrenched rivers. This entrenchment suggests that the rivers are unable to shift their course on their own [e.g., *Replumaz et al., 2001*], which is supported by the fact that the valleys have relatively symmetric cross sections. We thus consider that the half-width of the valleys provides the maximum uncertainty for the 2.5 km offset. Finally, the consistency between the three offsets suggests that all drainages recorded the same faulting period.

### 3.3. Kilometric Offset Along the Predjama Fault

#### 3.3.1. The Soča Valley

Important changes in the Soča River channel pattern and valley geometry can be observed where it crosses the Predjama fault. From NE to SW, the morphology of the Soča channel abruptly changes from a narrow gorge flanked by narrow strath and cut terraces standing between 50 and 80 m above the bedrock channel (black arrows in Figure 5a) to a wider valley floor composed of lower and wider terraces (Figures 2, 5a, and 6). This shift could indicate uplift of the northeastern part, resulting in enhanced incision. The Soča catchment, limited by the prominent Kanalski Kolovrat (KK) ridgecrest to the NW and by the edge of the Trnovski Gozd plateau to the SE, appears laterally shifted on both sides of the fault (Figure 5a). We therefore infer that the current geometry of the Soča Valley has recorded some right-lateral displacement along the Predjama Fault. The linear and well-preserved geometry of the KK ridgecrest was used to quantify the amount of cumulative offset. Drawing piercing lines along the two sections of the ridge yielded a value of 750 m when the proximal section of the ridge was considered and 1170 m when its entire length was considered (see red arrows in Figure 5a). Thus, we estimated an offset of  $960 \pm 210$  m. Back-slipping the fault section by this amount



**Figure 6.** (a) Soča channel morphology upstream of Avče looking northeastward. The deeply entrenched river is directly incising into the flysch bedrock along a narrow channel. (b) Westward view of the Avče terraces. Note the large valley and gently sloping hillslopes compared to the morphology observed a few hundred meters downstream (Figure 6b).

restores the initial catchment geometry and the course of the Soča (Figure 5b). Note that this cumulative displacement has been measured from the same marker than the 2.5 km offset along the Idrija Fault suggesting that the two have recorded the same period of time.

**3.3.2. The Čepovan Canyon**

Across the Trnovski Gozd Plateau, the Predjama Fault is marked by sharp topographical slope breaks and small karst basins that developed along its trace. These patterns are especially visible near the Čepovan Canyon, where the surface expression of the two fault branches is spectacularly preserved on the slowly evolving karstic landscape (Figures 3 and 7). The two branches symmetrically strike NNW on the right side of Figure 7, where they are respectively marked by the Mrzla Draga karstic depression and the Lokve Basin, a right-releasing step. Farther NW the two segments bend to the west along a N318 strike, where partitioning between the two segments has apparently controlled some subsidence in between (Figure 7a), marked by a 110 m high cumulative scarp along the northwestern branch (Figure 8).

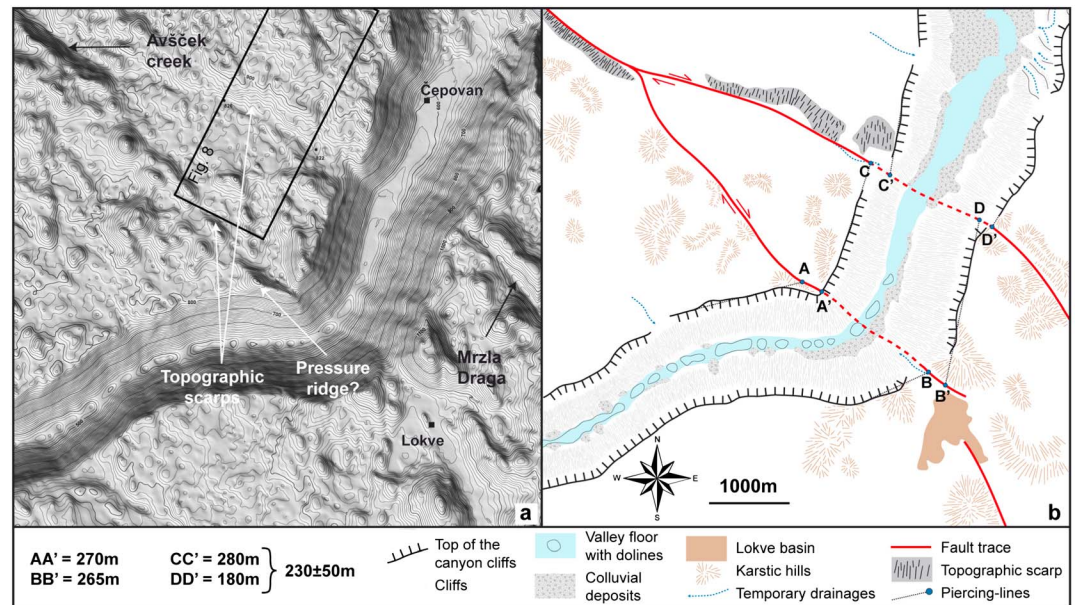


**Figure 7.** (a) Shaded 12.5 m DEM and (b) topography and geomorphic interpretation of the displaced morphologies along the Predjama Fault across the plateau and the Čepovan Canyon. Black dotted lines represent the piercing lines used to measure offsets. The black box in Figure 7a (labeled "Fig. 8") shows the area where topographic profiles were performed (Figure 8).

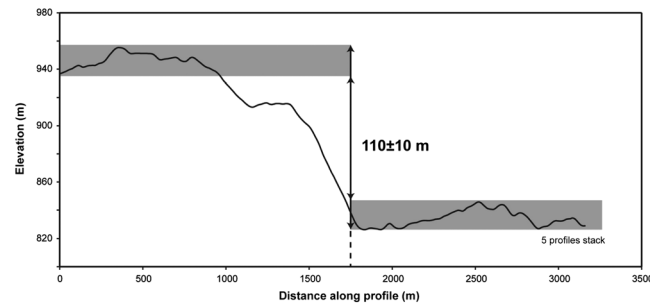


**Figure 8.** Stack of five parallel topographic profiles extracted from the 12.5 m DEMs. These profiles cross the northern branch of the Predjama Fault at right angles and show that the northeastern block was uplifted by 110 m.

The canyon is clearly offset along the northeastern fault segment. We estimate the offset from 180 to 280 m using piercing lines along the tops of the canyon cliffs (CC' and DD' in Figure 7). Along the southwestern branch, the eastern cliff appears to be right-laterally displaced by approximately 265 m (BB' in Figure 7), but the gully that extends the Lokve Basin disrupts the continuity of the cliff, preventing any robust interpretation. On the NW side, the trend of the canyon edge abruptly changes from N200 to N257 when crossing the fault.

Where the fault intersects the canyon, a conspicuous 500 m long N290 striking hill occurs, which could be interpreted as a pressure ridge associated with the right-lateral motion on the fault. If correct, this interpretation would imply that the western cliff has been displaced by ~270 m along the southwestern fault strand (AA' in Figure 7). The lack of apparent displacement in the canyon floor itself could be accounted for by the presence of slope colluvium at the base of the cliffs (Figure 7b).

Overall, these observations suggest approximately a total of 500 m of right-lateral faulting recorded by the Čepovan Canyon and distributed along the two branches of the Predjama Fault. The recorded displacement across Čepovan canyon appears significantly lower compared to the one recorded on the Soča Valley. This observation could possibly indicate that (1) the fault-bounded block is rotating (this scenario is illustrated in Figure 5b, assuming that the Čepovan Canyon has recorded the same amount of faulting than the KK ridgecrest) or (2) the offset of the Čepovan Canyon began to accumulate displacement later than the Soča Valley. The steep cliff morphology observed along the canyon has probably acted as a passive marker only since the abandonment of the Čepovan Canyon. Thus, the displacement preserved along the Predjama Fault most likely postdates abandonment. On the other hand, the Čepovan Canyon and the Soča Valley have recorded the same amount of horizontal motion along the Idrija Fault, which might represent the entire slip following the onset of canyon incision.

### 3.4. Evidence of Faulting- and Folding-Induced Upheaval From the Trnovski Gozd Plateau and Čepovan Canyon Topography

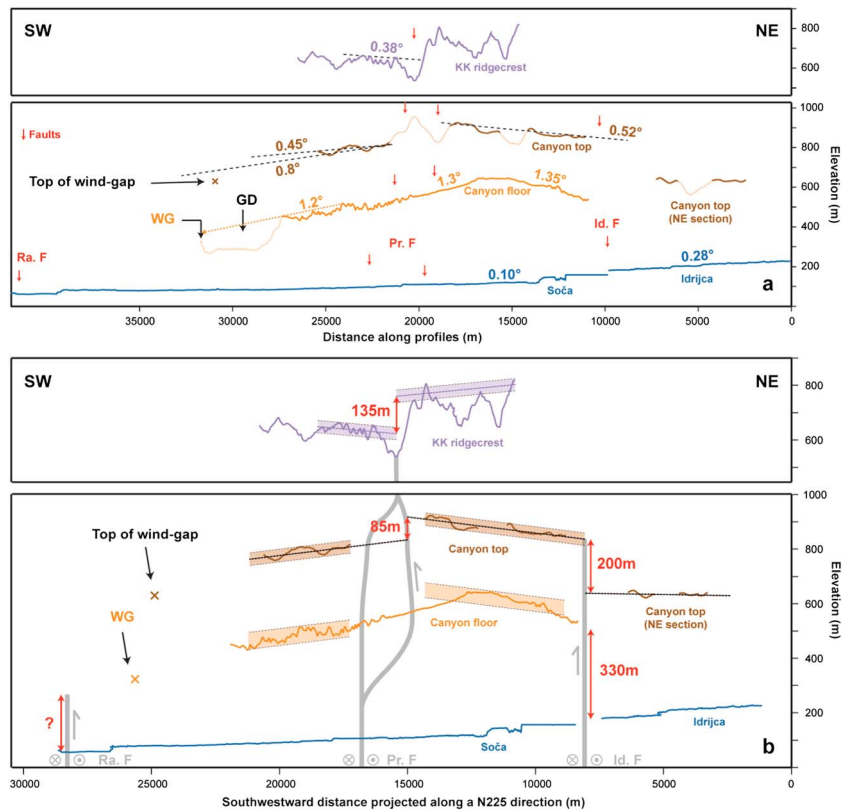
#### 3.4.1. Topographic Profiles of the Čepovan Canyon Top and Floor

Figure 9a represents the longitudinal topographic profiles of the Idrija Valley east of Dolenja Trebusa, the top Čepovan Canyon cliffs, the Čepovan Canyon floor, and the Kanalski Kolovrat (KK) ridgecrest. The canyon top profile is interrupted and displays a 200 m apparent throw across the Idrija valley. Moreover, all profiles except the ones of the present rivers exhibit sharp topographical steps at the location of the Predjama Fault. Finally, both the canyon floor and the canyon top cliff profiles show a bulging shape SW of the Idrija Fault.

In Figure 9b, the profiles were projected in the N225 direction (perpendicular to the mean N315 strike of the Dinaric faults) to quantify the vertical offsets observed across the Predjama and Idrija faults. A 200 m vertical component, corresponding to a relative uplift of the southwestern block, is inferred by extrapolating the canyon top cliff profile slopes up to the Idrija Fault (dotted lines in Figure 9b).

Moreover, on both sides of the Predjama Fault, the “canyon top” profile appears consistent with the 110 m vertical throw on the northeastern branch of the Predjama Fault on the plateau (section 3.3.2). Note that approximately 135 m of vertical throw across the Predjama Fault is also inferred from the KK ridgecrest profile (Figure 9b).

The “canyon floor” profile displays 330 m of apparent vertical uplift with respect to the modern Idrija channel at the position of the Idrija Fault (Figure 9b). This value indicates the maximum vertical displacement since canyon abandonment, which is in agreement with the vertical offset inferred from the “canyon top” profile. Although possibly buried by recent rockfall sediments (Figures 4 and 7), no clear vertical motion is observed across the Predjama Fault.



**Figure 9.** (a) Longitudinal profiles of the Idrjca and Soča Rivers, the floor and top of Čepovan Canyon, and the Kanalski Kolovrat ridgecrest. The canyon top profile has been extracted along the edges of the karstic surface, which top the Idrjca valley in the NE (labeled NE section in the figure) and the Čepovan Canyon in the SW (see Figure 3). The profile of the canyon top was smoothed from a 12.5 m DEM (200 m smoothing window). Light sections of the profile of the canyon top represent local hills or drainages and are not considered in the interpretations. The numbers indicate slope values. (b) The same profiles are projected along a N225 direction to quantify the vertical offsets on the faults. The transparent boxes used to quantify the vertical displacement of the canyon top across the Predjama Fault were shifted lower to highlight the rough equality of the canyon top and floor slopes. Ra. F = Raša Fault; Pr. F = Predjama Fault; Id. F = Idrjca Fault; WG = wind gap (see Figure 4); and GD = Grgar depression.

Finally, the wind gap elevation suggests that the canyon has been vertically displaced (the question mark in Figure 9b) across the Raša Fault with respect to its former outlet, the Soča River (section 3.1). Because the canyon does not cross the Idrijca and Raša Faults, bounds must be placed on the former canyon floor geometry to quantify its vertical offsets. Additionally, the impacts of nontectonic processes on the modern canyon morphology must be assessed.

### 3.4.2. Origin of the Warped Čepovan Canyon Topographic Profile and Constraints on the Former Canyon Slope

The possibility that the observed warped geometry of the Čepovan Canyon resulted only from river erosion processes can be ruled out by the three following observations: (1) as already noted by *Habič* [1997], the convex profile of the northward sloping section (Figure 9a) makes it difficult to believe that it was shaped by river incision; (2) no features, such as a ridgecrest, are present that might be associated with a former water divide near the maximum floor elevation; and (3) instead of two nested valleys, which would be expected if the opposite slopes resulted from a reversal of the flow direction, the canyon systematically displays a single V-shaped cross section. The most straightforward explanation for this morphology is that the present warping of the Čepovan Canyon resulted from tectonic deformation, i.e., from folding of the Čepovan Canyon. This supposed folding component, extending between the Idrijca and Raša Faults and controlling the observed uplift, is also supported by (1) a similar bulging shape at the top of the canyon profile (Figure 9b) and (2) the observed overdeepening of the Nadiža and Soča Rivers in the zone of maximum uplift halfway between the Idrijca and Predjama Faults (Figure 2). However, overdeepening was not observed in the canyon cross section near the assumed anticlinal hinge (Figure 3), suggesting that folding occurred after canyon abandonment.

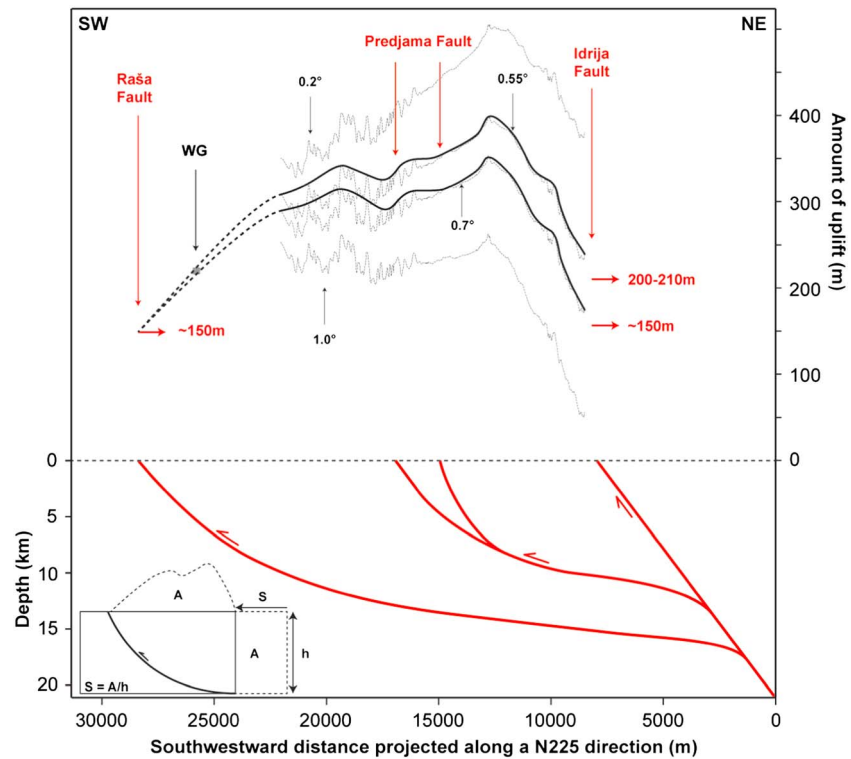


**Figure 10.** (top) Uplift profile (thin dashed lines) of the Čepovan Canyon considering different former slope values (black numbers). The thick black line represents the envelope profile approximating the fold geometry (the current profile of the canyon floor is pitted by numerous dolines, and the envelope curve is used to eliminate the effect of karstification by removing the high-frequency relief). The southwestern section of the envelope curve (thick dashed line) was constructed by extending the fold shape up to the Raša Fault through the Grgar wind gap. Red numbers indicate vertical displacements on the Idrija and Raša Faults. Ra. F = Raša Fault; Pr. F = Predjama Fault; Id. F = Idrija Fault; and WG = Grgar wind gap. (bottom) Fault geometry at depth inferred from the geological cross section (Figure 11). The horizontal scale is exaggerated by approximately 2 times with respect to the vertical scale. Inset shows the geometric parameters used for calculating the amount of shortening ( $S$ ) from the cross-sectional area ( $A$ ) of an uplifted geomorphic marker.

### 3.4.3. Uplift Profile of the Čepovan Canyon

Quantifying the amount of tectonic uplift and folding requires constraining the initial profile of the canyon that is just before abandonment. In Figure 3, point J represents the probable former junction between the Soča River and the Čepovan Canyon, lying roughly at the position of the Raša Fault. Because the surface area drained by the Soča River downstream from point J was not modified by canyon abandonment (compare Figures 5a and 5b) and given the large size of the watershed, we considered that the elevation of point J remained relatively constant over time, i.e., approximately at 75 m asl. Moreover, the black dotted lines in Figure 9b show that the dip of the “canyon top” fold limbs are similar to those of the “canyon floor” fold, suggesting that the canyon floor experienced most of the folding recorded by the plateau. This inference is also supported by the absence of overdeepening across the zone of maximum uplift (section 3.4.2). Both observations strongly indicate that the canyon floor and top recorded approximately the same amount of folding. From this observation, we assume that the floor/top folding ratio is at least 0.75 (the maximum value of 1 represents the same degree of folding in the canyon floor and top). Assuming contemporaneity of the folding- and fault-related vertical motions and considering the 200 m uplift recorded by the plateau across the Idrija Fault, the 0.75–1.0 range of the folding ratio implies that the northern tip of the canyon floor was vertically displaced by 150 to 200 m across the Idrija Fault. In Figure 10, different initial gradients (with point J remained fixed at the present elevation) have been cut from the modern profile of the Čepovan Canyon to construct the corresponding uplift profiles (dotted lines in Figure 10). A slope of between 0.55 and 0.7° is required to observe the 150–200 m uplift at the Idrija fault. The resulting profiles display two folds bounded by the three strike-slip faults that accommodated their growth and some vertical displacement. The vertical component was inferred to equal approximately 150 m at the position of the Raša Fault.

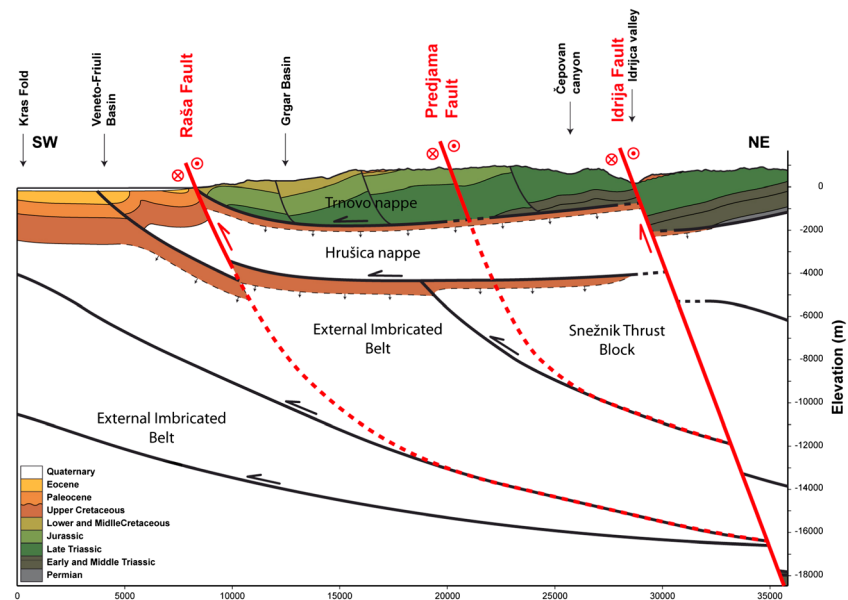


**Figure 11.** Geological cross section perpendicular to the average strike of the Dinaric faults along the profile shown in Figure 2b. The shallow geometry comes from *Buser [1968]* and *Buser et al. [1986]*, and the geometry of inactive thrusts at depth is adapted from *Placer et al. [2010]*.

### 3.5. Assessing the Deep Structure of the DFS and Quantifying Folding-Induced Shortening

#### 3.5.1. Geological Cross Section

A 36 km long geological cross section was constructed in the N220 direction from 4.2 km east of Kneža to 6.2 km SW of Gorizia (Figures 2 and 11). NE of the Raša Fault and along most of the section, the outcropping formations correspond to the Mesozoic rocks of the Trnovo nappe (thrust to the SW during the Eocene compression [*Placer et al., 2010*]). Along the 8 km long southwesternmost stretch, the alluvial sediments of the Veneto-Friuli Basin lie on the Cenozoic units of the Hrušica nappe and the external Dinarides fold-thrust belt, which are both Eocene-Oligocene in age [*Placer et al., 2010*]. The geometry of stratigraphic contacts and position of thrusts at the surface shown in Figure 11 come from *Buser [1968]* and *Buser et al. [1986]*. Dips of the Dinaric faults are documented as ranging between 60 and 80° toward the NE [e.g., *Poljak et al., 2000; Čar, 2010*], and faults are shown as dipping by 70°NE in the cross section.

The geometry of the inactive thrusts is controlled by two ductile horizons above and below the Mesozoic carbonate rocks of the Dinaric platform [*Placer et al., 2010*]. The lower horizon consists of clastic rocks of Permian to Lower Triassic age, whereas the upper horizon consists of Upper Cretaceous-Eocene flysch deposits. From two boreholes located at Cerčno and in the Adriatic offshore approximately 60 km WSW of Trieste, *Placer et al. [2010]* inferred the rough geometry of thrusts and decollement levels beneath the Northern Dinarides along a NE-SW cross section located approximately 20 km farther to the SE. Considering the locations of the two sections, we used a similar geometry in Figure 11. Folding across the Čepovan Canyon suggests that the Raša and Predjama Faults are probably connected to the Idrija Fault at depth. Thus, we propose that the Raša and Predjama Faults sole out from the same ductile horizons as the former Eocene-Oligocene thrust planes and that both are connected to the Idrija Fault in the NE. This geometry implies that the Raša Fault would merge with the frontal thrusts of the external Dinarides and that the Predjama Fault would merge with the Snežnik thrust (Figure 11). Alternatively, the Predjama Fault could cross and cut the Snežnik thrust and connect with deeper ductile horizons. Based on these hypotheses, the decollement levels lie at approximate depths of 10 to 17 km, which agrees with the estimated depth of the base of the seismogenic layer proposed in the area at depth of 10 to 15 km [*Poljak et al., 2010*]. Finally, the deep geometry of the DFS is similar to a transpressive half-flower structure centered on the Idrija Fault. This composite structure would control the uplift and folding of the crustal wedge between the Idrija and Raša Faults.

#### 3.5.2. Čepovan Canyon Shortening Determination

The extreme bounds of the uplift profiles have been redrawn to account for the chaotic geometry resulting from karstic erosion (thick black curves in Figure 10) (note that a small bulge appears between the two

Predjama Fault segments). The inferred fold geometry appears asymmetrical, with a steeper northeastern limb (Figure 10). To deduce the amount of shortening recorded by the Čepovan Canyon, we assumed conservation of mass [see, e.g., Lavé and Avouac, 2000] (inset in Figure 10).  $A$  is the cross-sectional area of the profile corresponding to folding-induced uplift, and  $h$  is the thickness of the crustal unit sliding above the basement and folding at the surface (inset in Figure 10). If plane strain and conservation of mass are assumed, the amount of shortening,  $S$ , can be deduced from the following relationship:

$$S = A/h$$

The cross-sectional area,  $A$ , was calculated from the uplift profiles and was  $5.84 \pm 0.30 \text{ km}^2$ . Considering the depth of the decollement,  $h$ , between 12 and 15 km (Figure 11), a shortening ranging from 370 to 510 m is yielded.

The following results were obtained from the analysis of the large-scale geomorphic markers across the Idrija, Predjama, and Raša Faults. Following the deepening of the major drainages and the abandonment of the former alluvial plain on the Trnovski Gozd plateau, approximately 2.5 km of right-lateral displacement occurred along the Idrija Fault. Simultaneously, the gradually karstified alluvial plain was vertically displaced by approximately 200 m by the Idrija Fault. Because all the geomorphic markers used in estimating offsets are roughly coeval (sections 3.2, 3.3.1, and 3.4.3) it is assumed that during the same period, the Predjama Fault laterally slipped by  $960 \pm 210 \text{ m}$  and controlled (together with the Raša Fault) the folding and uplift of the karstified areas of the Trnovski Gozd plateau and of the Čepovan Canyon floor, accounting for  $440 \pm 70 \text{ m}$  of strike-perpendicular shortening.

In comparison, the total displacements along the Idrija and Predjama Fault segments observed from geological maps suggest 4–5 km along the Idrija fault and no more than 1 km offset, respectively (Figure 2a). More accurate estimates presented in supporting information Text S1 indicate  $4.7 \pm 0.7 \text{ km}$  and  $1040 \pm 120 \text{ m}$  for the Idrija and Predjama Faults, respectively, and a maximum displacement of approximately 1030 m for the Raša Fault. Note that along the Idrija Fault, the total vertical displacement appears similar to the one derived from the topography of the Čepovan Canyon top and floor (see supporting information Text S1). While the geomorphic displacement along the Idrija Fault represents approximately half of the estimated geological offset, the large-scale morphology appears to capture the entire slip along the Predjama Fault. This observation indicates that the inception of slip along the Predjama Fault occurred not before the 2.5 km offset began to accumulate along the Idrija Fault.

The objective of the next section is to accurately constrain the late Pleistocene slip rates of these faults by quantifying the magnitude and timing of the most recent motion from recent morphological markers. This assessment will allow for discussions of the time variability in the fault kinematics along the DFS.

#### 4. Late Pleistocene Cumulative Offsets and $^{36}\text{Cl}$ Cosmic Ray Exposure Ages of the Displaced Markers

In this section, we focus on smaller displacements ranging from a few meters to about 350 m to estimate the late Pleistocene slip rates of the Dinaric Faults. The rates were derived by combining  $^{36}\text{Cl}$  cosmic ray exposure (CRE) ages of displaced markers with existing glacial and alluvial chronologies of the area. We first describe the method used for determining  $^{36}\text{Cl}$  CRE ages then present the sites that allowed constraining slip rates along the three main Dinaric faults.

##### 4.1. Methods Used for Determining the $^{36}\text{Cl}$ CRE Ages of Displaced Geomorphic Markers

The displaced geomorphic markers presented in the following sections are mainly composed of limestone. The ages of emplacement of some of those markers were determined by measuring the amounts of cosmogenic  $^{36}\text{Cl}$  produced in situ. Samples were either pieces of bedrock (river-cut cliffs and cut terrace) or pebbles deposited on alluvial strath terraces. All samples were crushed, and 250–500  $\mu\text{m}$  fractions of each sample were leached and then dissolved following the procedure described by Stone *et al.* [1996] and modified by Schlagenhauf *et al.* [2011]. After complete dissolution, the samples were spiked with a known amount of isotopically enriched stable chloride carrier to allow for simultaneous Cl and  $^{36}\text{Cl}$  determination by isotope dilution [Schlagenhauf *et al.*, 2011, and references therein]. Then, Cl was precipitated as AgCl. Both [ $^{36}\text{Cl}$ ] and [Cl] were measured at the national French Accelerator mass spectrometry facility (Accélérateur pour les Sciences de la Terre, Environnement, Risques; Centre Européen de Recherche et d'Enseignement des Géosciences de

l'Environnement, ASTER-CEREGE, Aix-en-Provence). The  $^{36}\text{Cl}$  and Cl concentrations were normalized to a  $^{36}\text{Cl}$  standard prepared by K. Nishiizumi (KNSTD1600, with a given  $^{36}\text{Cl}/^{35}\text{Cl}$  value of  $(2.11 \pm 0.06) \times 10^{-12}$ ) [Sharma *et al.*, 1990; Fifield *et al.*, 1990]. The decay constant of  $2.303 \pm 0.016 \times 10^{-6} \text{ yr}^{-1}$  used corresponds to a  $^{36}\text{Cl}$  half-life ( $T_{1/2}$ ) of  $3.014 \times 10^5$  years. The analytical uncertainties included counting statistics, machine stability and blank correction. [Ca] was also measured in sample aliquots by using inductively coupled plasma-atomic emission spectrometry (ICP-AES) analyses to determine the  $^{36}\text{Cl}$  concentrations produced from this target element. The Stone [2000] polynomial was used to determine the local production rates from the  $42.2 \pm 4.8 \text{ atoms/g Ca/yr}^{-1}$  production rate provided by Schimmelpfennig *et al.* [2011]. Finally, the Excel spreadsheet provided by Schimmelpfennig *et al.* [2009] was used to calculate all of the  $^{36}\text{Cl}$  production pathways.

#### 4.1.1. Density of Sampled Material

At two sites, samples were either buried beneath a 150 cm thick colluvial deposit or distributed along heterogeneous (limestones pebbles and fine-grained matrix, capped by a 20–50 cm thick soil) 2 m deep profiles. To consider the decrease in the  $^{36}\text{Cl}$  production rate with depth, the density of the material was estimated using typical densities ( $1.5 \text{ g/cm}^3$  for the soils and  $2.1 \text{ g/cm}^3$  for the colluvium) and the relative amounts of pebbles and matrix observed in the profiles ( $2.7 \text{ g/cm}^3$  for the density of limestone pebbles). An attenuation length of  $160 \text{ g/cm}^2$  was used [Gosse and Phillips, 2001], and the compositions of the sampled markers and the densities used to calculate the exposure ages are listed in the supporting information in Table S1 and Text S2.

#### 4.1.2. Denudation Rates and Steady State Equilibrium

Generally, if the samples reached steady state equilibrium (their ages are old enough such that the concentration gains through production are balanced by the concentration losses through radioactive decay and surface denudation, which implies that the  $^{36}\text{Cl}$  concentration depends only on the denudation rate [Gosse and Phillips, 2001]), the calculated exposure ages must be considered only as minimum ages. The steady state hypothesis was tested in our samples by determining the denudation rates that were compatible with infinite exposure ages. At all sites, denudation rates between 150 and 500 mm/yr were deduced. These values were much higher than the published estimate of denudation rates in carbonate environments (approximately 20 mm/ka; e.g., Ryb *et al.* [2014] and Sadier *et al.* [2012]). Therefore, the samples are not at the steady state, and their concentrations can be used to determine the CRE ages.

#### 4.1.3. Chlorine Concentration and Neutron Capture Production Uncertainties

If high (more than 50 ppm), the chlorine concentrations in the samples could represent a significant source of uncertainty because of the poorly constrained fluxes of thermal and epithermal neutrons that produce  $^{36}\text{Cl}$  through neutron capture [e.g., Schimmelpfennig *et al.*, 2009; Delunel *et al.*, 2014]. At one of the three sites, the chlorine concentrations range between 72 and 155 ppm (Table 1). Because these uncertainties are difficult to quantify, we conservatively used an absolute uncertainty of 30% to deduce the CRE ages at this site.

#### 4.1.4. Depth Profile Modeling

The  $^{36}\text{Cl}$  concentration along the profile depends on the surface denudation rate, the inheritance, the density of the deposit (which controls the depth of attenuation), and the exposure duration. When samples were collected with depth, the concentrations were modeled either by varying all four parameters [Braucher *et al.*, 2009] or by fixing some of the parameters to test their respective influences on the resulting CRE ages. The best fit was determined by using a chi-square ( $\chi^2$ ) inversion [e.g., Siame *et al.*, 2004; Braucher *et al.*, 2009]. Because the  $^{36}\text{Cl}$  production rate depends on the individual chemical compositions of each sample, the  $^{36}\text{Cl}$  concentrations plotted on the profiles were normalized to a standard chemical composition, which was chosen based on one of the measured samples.

### 4.2. Cumulative Displacements and $^{36}\text{Cl}$ CRE Ages Along the Idrija Fault

#### 4.2.1. The Idrija-Godovič Segment

We first focused on the region between Idrija and the area a few kilometers SE of Godovič. This 11 km long segment of the Idrija Fault runs along the transition between the karstic areas to the SE and the deep gorges of the Idrija catchment to the NW (Figure 2b). SSE of Godovič, the relief comprises two main karstic levels (S1 and S2 in Figure 12), which were eroded in some places by drainage-like features in the form of poorly incised dry channels (the most prominent one is the Godovič karstic drainage approximately 400 m east of Godovič). To the NW, this karstic tableland was deeply incised by the Zala River. The active trace of the Idrija Fault is well expressed in the morphology along most of the section presented in Figure 12. In the SE, it is first marked by a sharp continuous and linear topographical step (not associated with a change in lithology) that affects the S1 level, which could be interpreted as a cumulative fault scarp. Farther to

**Table 1.** General Sample Information, Measurements ( $^{36}\text{Cl}/^{35}\text{Cl}$  and  $^{35}\text{Cl}/^{37}\text{Cl}$  Ratios and Chlorine and CaO Concentrations), and Calculated  $^{36}\text{Cl}$  and Chlorine Concentrations<sup>a</sup>

Site	Sample	Latitude (°N)	Longitude (°E)	Elevation (m)	$^{36}\text{Cl}/^{35}\text{Cl}$ ( $\times 10^{-14}$ )	$^{35}\text{Cl}/^{37}\text{Cl}$	$^{36}\text{Cl}$ ( $\times 10^4$ atoms/g)	Cl (ppm)	CaO (%)	CRE age (ka)
Anžic site	Je 12-1	45.9733	14.0762	471	3.50 ± 0.23	5.16 ± 0.05	8.35 ± 0.56	115	35.1	4.6 ± 0.5
	Je 12-2	45.9733	14.0762	471	3.90 ± 0.47	5.85 ± 0.02	8.46 ± 1.01	92	37.4	4.9 ± 0.7
	Je 12-3	45.9733	14.0762	471	2.95 ± 0.27	7.00 ± 0.07	7.73 ± 0.72	95	36.9	4.4 ± 0.5
	Je 12-4	45.9733	14.0762	471	5.59 ± 0.32	5.23 ± 0.03	14.63 ± 0.85	123	35.3	7.9 ± 0.8
	Je 12-1'	45.9733	14.0762	471	4.27 ± 0.29	5.98 ± 0.04	9.78 ± 0.68	95	34.5	8.3 ± 0.9
	Je 12-2'	45.9733	14.0762	471	4.60 ± 0.34	4.90 ± 0.01	14.16 ± 1.06	155	35.4	10.0 ± 1.1
	Je 12-3'	45.9733	14.0762	471	5.29 ± 0.32	6.30 ± 0.02	9.72 ± 0.58	72	32.9	9.3 ± 0.9
	Je 12-4'	45.9733	14.0762	471	6.79 ± 0.36	6.83 ± 0.02	17.47 ± 0.93	92	35.8	14.7 ± 1.4
PF	PF13-8	46.0384	13.9386	422	4.71 ± 0.28	8.75 ± 0.08	8.73 ± 0.53	38	31.9	14.2 ± 1.9
	PF13-11	46.0384	13.9386	422	4.59 ± 0.44	13.79 ± 0.12	9.66 ± 0.11	49	39.1	12.7 ± 2.1
Avče T1 terrace	PR13-1	46.1073	13.6781	184	8.13 ± 0.36	15.83 ± 0.22	8.38 ± 0.39	12	54.2	5.9 ± 0.6
	PR13-2	46.1073	13.6781	184	7.29 ± 0.34	9.76 ± 0.09	9.90 ± 0.47	30	55.6	5.4 ± 0.6
	PR13-3	46.1073	13.6781	184	6.22 ± 0.30	13.16 ± 0.16	7.27 ± 0.36	18	52.0	5.7 ± 0.6
	PR13-4	46.1073	13.6781	184	3.23 ± 0.21	29.12 ± 0.68	5.18 ± 0.36	6	55.2	6.3 ± 0.8
	PR13-5	46.1073	13.6781	184	1.60 ± 0.15	28.27 ± 0.93	3.64 ± 0.36	13	55.0	5.3 ± 0.8
	PR13-6	46.1073	13.6781	184	4.60 ± 0.29	10.44 ± 0.09	4.76 ± 0.30	22	54.5	6.1 ± 0.9
	PR13-7	46.1073	13.6781	184	5.97 ± 0.29	23.87 ± 0.45	5.13 ± 0.26	5	55.0	6.8 ± 1.0
	PR13-8	46.1073	13.6781	184	2.49 ± 0.20	16.62 ± 0.20	3.35 ± 0.28	17	55.8	6.6 ± 1.0
	PR13-9	46.1073	13.6781	184	6.29 ± 0.34	7.21 ± 0.11	4.55 ± 0.25	23	51.5	6.4 ± 0.9
	PR13-10	46.1073	13.6781	184	9.37 ± 0.41	16.28 ± 0.36	11.28 ± 0.55	13	52.8	11.6 ± 1.4
	PR13-11	46.1073	13.6781	184	11.34 ± 0.44	7.26 ± 0.09	8.34 ± 0.34	23	55.0	15.5 ± 2.6
	PR13-12	46.1073	13.6781	184	5.39 ± 0.31	8.45 ± 0.08	3.61 ± 0.21	18	52.7	7.7 ± 1.4
	PR13-13	46.1073	13.6781	184	1.42 ± 0.14	16.40 ± 0.39	2.07 ± 0.21	25	34.7	7.9 ± 1.6
Avče T1' terrace	PR13-15	46.1066	13.6793	174	5.39 ± 0.37	21.64 ± 0.24	9.24 ± 0.65	12	55.6	8.6 ± 1.1
	PR13-16	46.1066	13.6793	174	8.05 ± 1.08	13.52 ± 0.79	10.39 ± 1.52	19	55.7	9.7 ± 1.8
	PR13-17	46.1066	13.6793	174	5.82 ± 0.35	22.07 ± 0.45	5.52 ± 0.35	6	55.4	6.9 ± 1.0
	PR13-18	46.1066	13.6793	174	3.54 ± 0.27	22.34 ± 0.34	1.51 ± 0.12	3	24.0	5.3 ± 0.9
	PR13-20	46.1066	13.6793	174	4.59 ± 0.26	20.23 ± 0.35	3.47 ± 0.20	6	55.4	10.2 ± 2.0
	PR13-21	46.1066	13.6793	174	7.02 ± 0.33	9.51 ± 0.12	8.80 ± 0.43	29	54.9	5.9 ± 0.6
	PR13-22	46.1066	13.6793	174	4.60 ± 0.27	8.46 ± 0.11	3.73 ± 0.22	22	54.5	10.4 ± 2.1

<sup>a</sup>The CRE ages are apparent ages and were calculated according to Schimmelpfennig et al. [2009]. More information on sample chemistry is given in the supporting information, Table S1.

the NW and near Anžic, the fault cuts across the topography, apparently dragging an E-W oriented ridgecrest (arrow labeled "A") toward the NW and right-laterally displacing the Zala Valley (Figure 12). Farther to the NW, the fault crosses the Zala/Ljubevščica water divide to slightly bend toward the west. Before reaching the Idrijca Valley, the fault is marked by a topographic break, where small ridgecrests stop (arrows labeled "B" and "C" in Figure 12), in the Ljubevščica hillslope. When it reaches the Idrijca Valley, the fault splays into three right-stepping fault strands and becomes less clear, although the Idrijca river-cut cliff could be offset along the main branch of the fault (arrow labeled "D" in Figure 12).

Cumulative offsets have been identified and quantified at two sites along this section. The first one, which is not further presented, is the sharp dogleg made by the Godovič karstic drainage across the fault scarp corresponding to a 110 m long right-lateral offset (red arrow in Figure 12). The second site, which will be discussed in detail, is located in the Anžic area and affects the Zala Valley (black box in Figure 12).

NE and SW of Anžic, the Zala River generally flows toward the SW (Figures 12 and 13). The Zala River is slightly entrenched by 1–2 m in a 50–60 m wide valley floor (appearing in green in the slope map; Figure 13a), which narrows to a width of 25 m downstream of the fault. This valley floor, which is made of a single alluvial surface (S1 in Figure 13b), is bounded by steep hillslopes (slope angle = 30–45°, Figure 13a) cut into massive dolomites along a 1 km long section on both sides of the fault. Farther to the SW, this 600 m long narrow valley section becomes wider, reaching approximately 400 m downstream of the fault where the Zala is fed by first-order tributaries that have incised into more clay-rich rocks (southwestern corner of Figures 13a and 13b).

In the middle of the studied section, the Zala Valley is deflected to the NW when crossing the fault. A prominent ridgecrest that separates the Zala and the Okroglica streams downstream of the fault reveals a similar

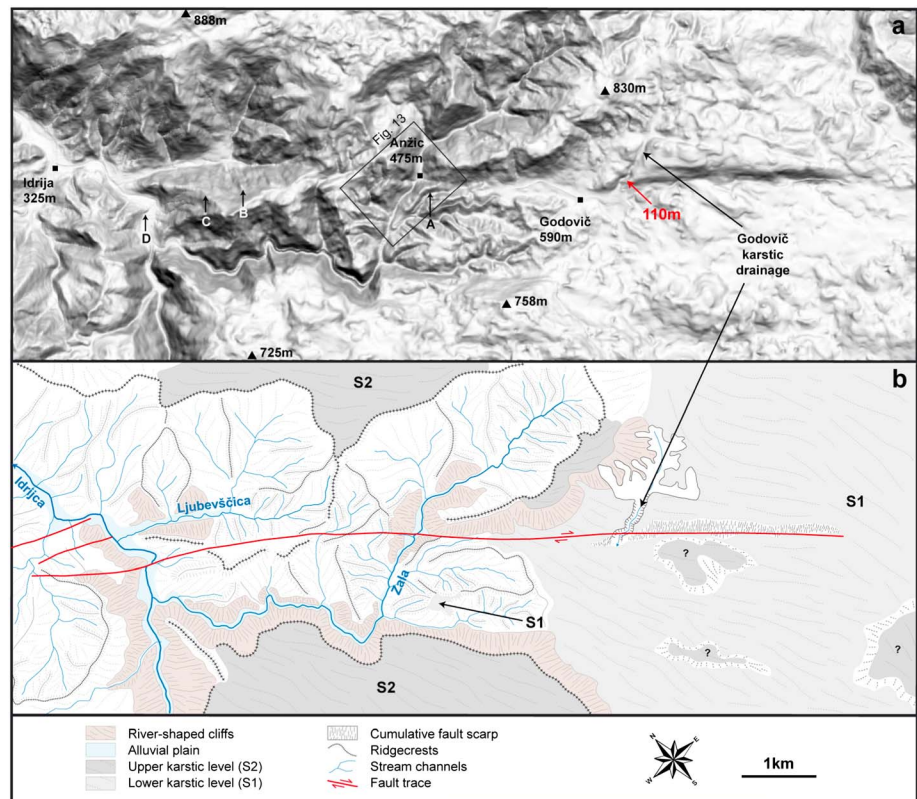


**Figure 12.** (a) Shaded 12.5 m DEM of the Idrija-Godovič Fault segment exhibiting surface expression of recent motion. The small red arrow is related to features mentioned in the text. (b) Geomorphic interpretation of Figure 12a. (Note that a tributary of the Zala is apparently deflected by approximately 500 m along the fault approximately 1 km NW of Godovič. The large amount of lateral shift in the course of this small stream compared to the smaller displacements recorded by the other larger rivers suggests a nontectonic origin. We prefer to interpret this feature as stream capture, which would explain the observed tightening of its catchment along the fault).

geometry suggesting that it has been dragged along the fault (Figures 12a, 13a, and 13b). A 100 m long 60 m wide flat surface (S2 in Figure 13b), standing approximately 25 m above the present Zala channel, is exposed downstream of the fault and on the north bank of the river, where it has been sheltered from river erosion. In the field, this surface is covered by dense vegetation and is dissected by small and narrow gullies drained by the Zala. This surface lies in the prolongation of the linear downstream section of the Zala and is located where the present Zala Valley floor reaches its minimum width (Figures 13a and 13b).

From these observations, we inferred that the former course of the river flowed across S2, which represents an abandoned terrace of the Zala. Consequently, S2 and the river-cut cliffs would have been incrementally displaced by right-lateral slip along the fault. When the incision power of the Zala became high enough, it abandoned S2 and shaped a new channel (the present one) to the SE to restore a more linear course (Figure 13b). The last stage was the return to low incision power, which led to the accumulation of right-lateral displacement of this new channel (itself accommodated by enhanced lateral erosion) with respect to the upstream section of the valley (Figure 13a). This scenario explains most of the observations, such as the observed offsets, the slope distribution, and the narrowing of the valley floor downstream of the fault.

Quantifying the cumulative offset recorded by the Zala Valley requires making assumptions on the initial valley geometry in the vicinity of the fault. The most relevant observation is that the valley differs from the very linear geometry observed upstream and downstream only along a 200 m long section downstream from the fault where the S2 surface has been abandoned then preserved. This strongly suggests that this less linear section has resulted from lateral motion along the fault. Assuming that the valley were initially completely linear over the entire section of Figure 13 (which would imply that S2 was no more laterally extensive in the past) allows quantifying an offset of about 135 m from the north bank of the river (AA' in Figure 13b).

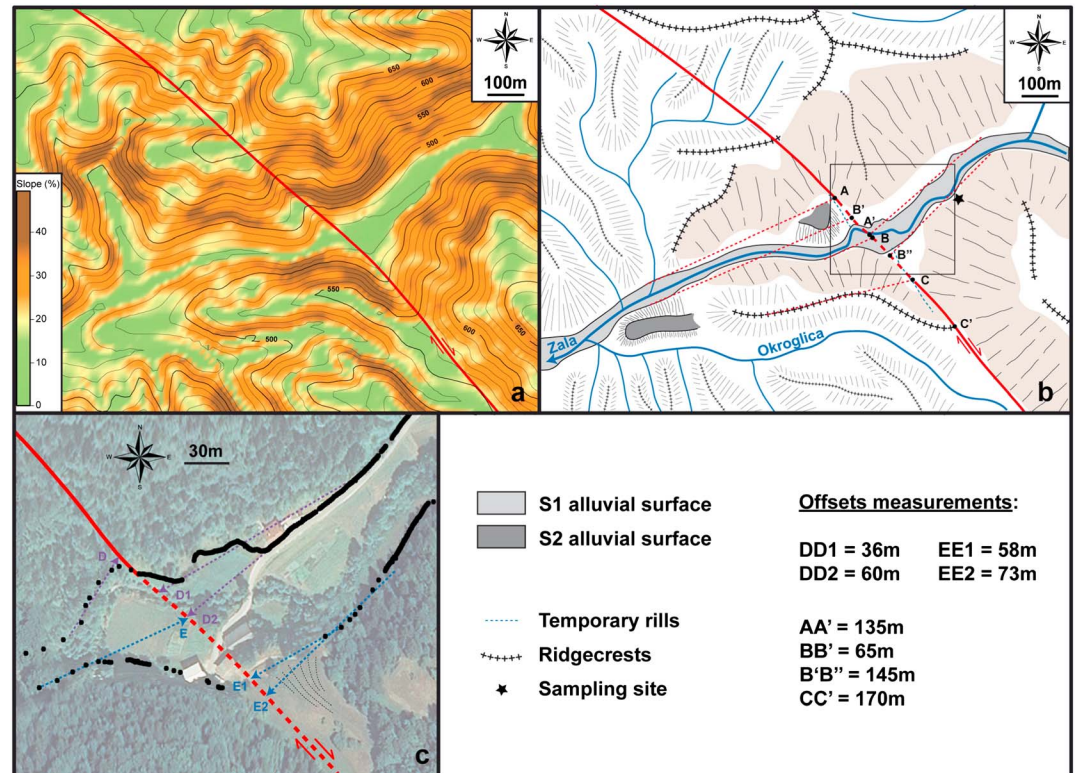


**Figure 13.** (a) Slope map of the Anžic site. Note the enhanced slopes on the right hillslope NE of the fault and on the left hillslope SW of the fault, the narrowing of the valley floor (which appears in green) SW of the fault, and the small green patch of the preserved alluvial surface in the middle of the figure. The red line represents the trace of the Idrinja Fault. (b) Geomorphic interpretation of the Anžic site showing the wrench shape of the Zala Valley floor and the preserved S2 surface just to the SW of the fault. Red dotted lines represent the piercing lines estimating the geometry of the river banks and are used to measure the cumulative offsets. The black star shows the location of the sampling site, and the black box shows the extent of Figure 13c. (c) A 50 cm orthophoto of the Zala Valley floor. Black points were acquired using kinematics GPS by following the edges of the valley. Purple and blue dotted arrows represent piercing lines used to measure offset. Thin black lines in the south represent colluvium covering the former edge of the valley. Upstream from the fault and on the right bank we were not able to follow the entire edge of S1 because of the house built at the base of the hillslope. According to the rest of the acquired points and the observed morphology in the field, it is likely that the rim of the valley runs just NW of the house (piercing line D1). To account for the high lateral erosion observed on this riverbank, we also defined an upper boundary for the intersection of the edge of the valley floor with the fault trace (piercing line D2). On the left bank, the intersection of the geomorphic marker with the fault trace was uncertain because the S1 geometry was partly reshaped by the along-fault-drained stream and its associated 30 m wide colluvium deposit (Figures 13b and 13c). Thus, we defined two extreme solutions with piercing lines E1 and E2.

Conversely, if assuming that S2 has been significantly laterally eroded, a minimum offset of about 65 m could be quantified (BB' in Figure 13b) by considering that S2 formerly extended up to the current south bank (piercing line B in Figure 13b). This latter scenario would imply that the present-day geometry of the valley is very similar to the one before S2 was abandoned. Finally, the deflection of the wrenched ridgcrest observed downstream from the fault yields a displacement of approximately 170 m. Since BB' only yields a minimum displacement and because CC' is relatively consistent with AA' we infer that the north bank of the river provides a better estimation of the cumulative offset. However, significant uncertainties arise from the assumption on the initial geometry of the valley; therefore, an uncertainty of 30% has been arbitrarily affected to this offset, yielding a value of  $135 \pm 40$  m.

Following our interpretation, at a certain time after the  $135 \pm 40$  m offset began to accumulate, a new channel, shifted to the SW to restore a more linear course, has incised across S2. This recent channel (black line in Figure 13b) filled by the S1 surface is itself laterally displaced along the fault. To constrain this displacement, a survey of the edge of S1 on both sides of the fault has been performed using a kinematic GPS (Figure 13c). From the S1 geometry, a right-lateral offset ranging between 36 and 73 m was inferred, with a preferred value

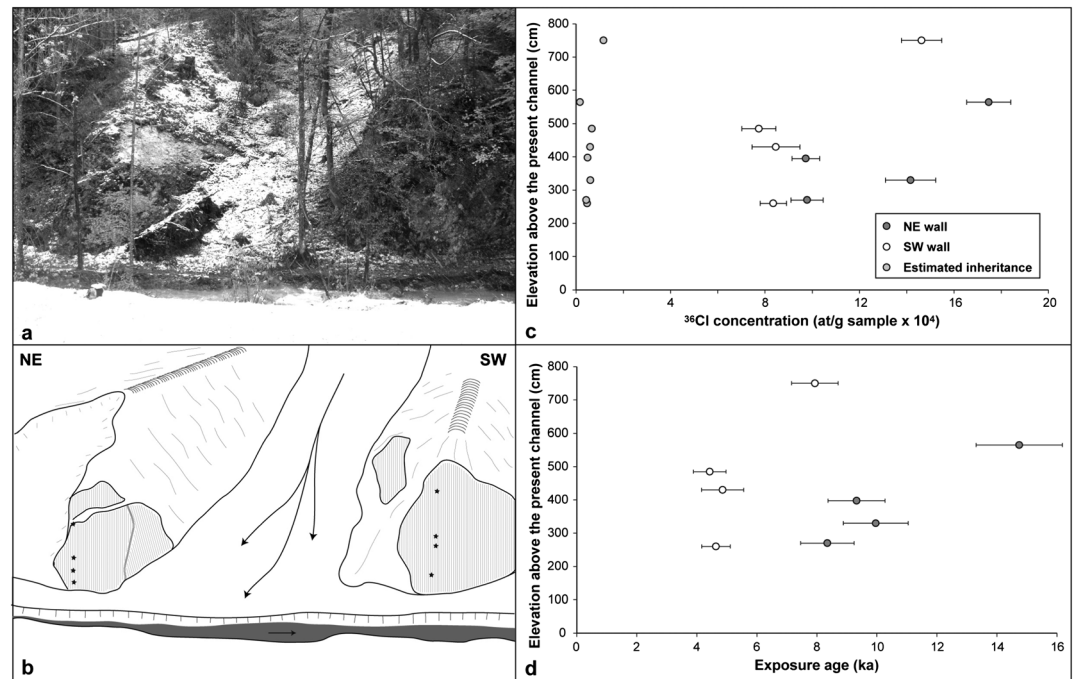


**Figure 14.** (a) Field photograph showing the sampled river-cut cliffs. (b) Sketch of the picture with the sampling locations shown with black stars. (c)  $^{36}\text{Cl}$  concentrations of the samples with height and the assessed  $^{36}\text{Cl}$  inheritance (see text for details). (d) Apparent CRE ages of the samples.

of  $48 \pm 12$  m yielded by the best preserved north bank (Figure 13c). Because S1 clearly corresponds to the active flood plain and cannot provide any relevant constraint on the timing of this offset, we focused on the markers of the incision event. The  $48 \pm 12$  m offset should have formed following the major incision event that resulted in the abandonment of S2 (and the creation of the new channel) about 25 m above S1. Therefore, we attempted to constrain the chronology of this incision to assign an age to the  $48 \pm 12$  m offset. Direct evidence of channel downcutting resulting from this incision event could be found about 250 m upstream from the fault in the form of two pieces of a river-cut cliff (Figures 14a and 14b and black star in Figure 13b). The cliff is approximately 8 m tall above S1 (Figure 14).

**$^{36}\text{Cl}$  Dating.** The two walls of the cliff were sampled for  $^{36}\text{Cl}$ -based CRE dating. Eight pieces of bedrock (four on each wall) were collected along vertical profiles from 270 to 750 cm above the present channel. Here the strategy is not to determine the age of S2 abandonment along a depth profile but to capture the signal of  $^{36}\text{Cl}$  production at the surface of the river-cut cliff, that is, the cosmogenic production when the vertical walls have been exposed by channel downcutting [see Saillard *et al.*, 2014]. To do so, we considered that the 25 m relative elevation of S2 provides the approximate amount of incision relative to the former and stable base level (that is S2). Assuming a stable base level duration of  $10^5$  years (approximately the duration of one glacial-interglacial cycle, which is believed to control the main incision phases), the  $^{36}\text{Cl}$  concentrations were calculated at the corresponding depths (that is, the depth below the S2 surface) of the samples for a  $10^5$  year period. The calculation yields  $^{36}\text{Cl}$  concentration ranging from  $1.10^3$  to  $1.10^4$  atoms/g of rock, providing a rough estimation of the inherited cosmogenic content (Figure 14c).

Samples from the river-cut cliff yielded [ $^{36}\text{Cl}$ ] ranging from  $7.73 \cdot 10^4$  to  $1.75 \cdot 10^5$  atoms/g of rock (approximately 10 times higher than that measured in the blanks,  $10^4$  atoms of  $^{36}\text{Cl}$ ) (see Table 1), at least 10 times higher than the estimated inheritance, and the values roughly increase with elevation (Figure 14c). The apparent CRE ages between 4.4 and 14.7 ka (Figure 14d and Table 1) represent the minimum ages of the incisional event because the cliff is an active marker that was potentially refreshed by lateral erosion by the Zala River. Along the northeastern wall, the ages mostly increase with elevation above the channel. Along the southwestern wall, this correlation is less clear and the CRE ages are systematically younger (Figure 14d). This observation suggests that postincision processes did not significantly affect the cosmogenic content

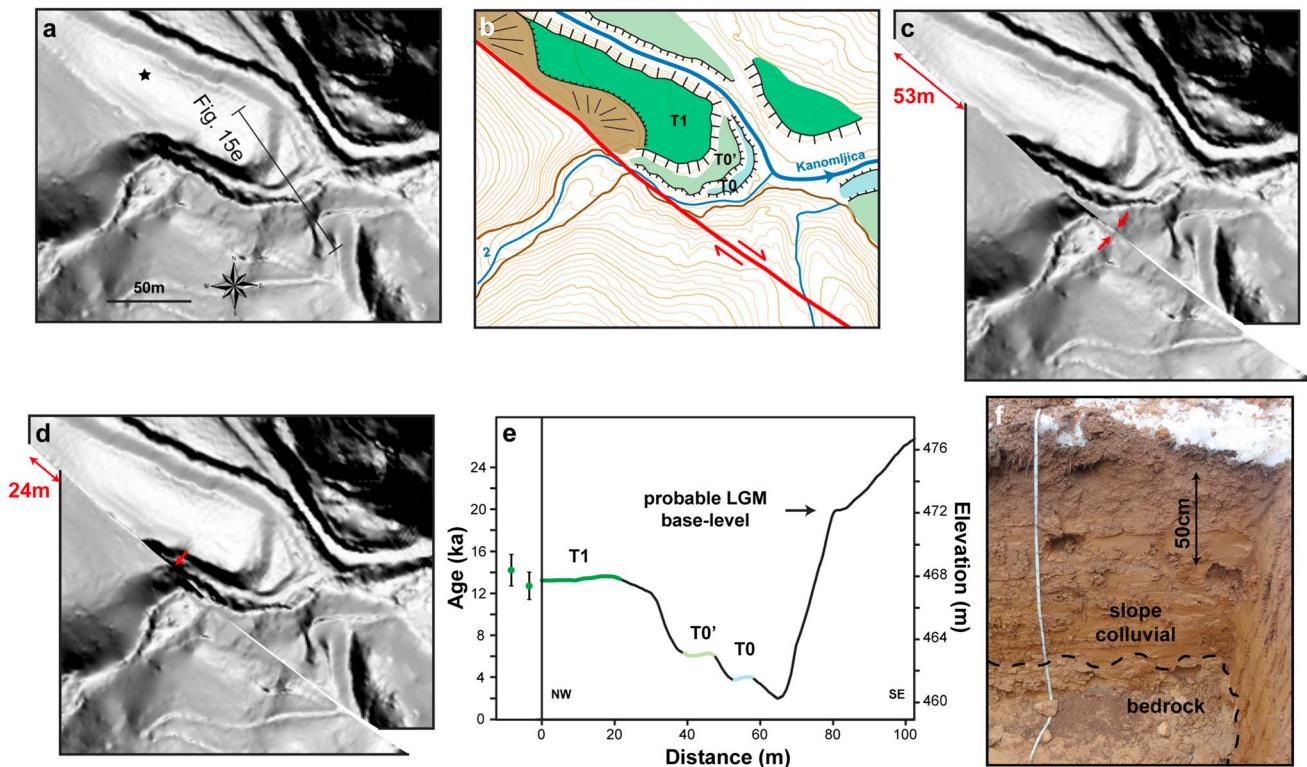


**Figure 15.** (a) One-meter lidar DEM and (b) geomorphic interpretation of the site and (c) 53 m and (d) 24 m back-slipping of the 1 m lidar DEM along the studied fault section. Red arrows show the restored continuity of the base of the river-cut cliff and the colluvium with the hillslope. (e) Topographic cross section of the stream 2 valley showing the elevations of alluvial surfaces and the notch at the top of the river-cut cliff. Apparent ages of the two bedrock samples are shown on the left of the figure. (f) Field photograph of the sampling ditch showing the colluvial deposit capping the bedrock (the boundary between the two is shown by the black dashed line); the two holes in the colluvial correspond to the positions and sizes of the angular pebbles.

on the northeastern wall but potentially rejuvenated the bedrock surface of the southwestern wall. Thus, the CRE age associated with the northeastern cliff most likely provides a good estimate of the minimum age of the incisional phase. Therefore, the actual channel would have begun to deepen before 14.7 ka. The implications in terms of slip rate assessment will be discussed with other dates in section 5.1.

#### 4.2.2. The Kapa Segment

The Kapa segment was previously investigated and described by *Moulin et al.* [2014]. At Pri Fežnarju (Figure 15; see location in Figure 2b), these authors constrained a  $53 \pm 5$  m right-lateral offset of first-order streams along a 1.5 km section of the Idrija Fault. Here we focus on the clearest offset that was recorded at this site and attempt to obtain dates using  $^{36}\text{Cl}$  produced in situ. Figure 15 shows the 1 m lidar DEM of the corresponding area and the morphotectonic interpretation (see details in *Moulin et al.* [2014]). In this interpretation, the T1 terrace, which is capped by a colluvial wedge, corresponds to a cut terrace shaped in the carbonate bedrock thus corresponding to a previous base level in which stream 2 merged with the Kanomljica River. Although T1 is only exposed NE of the fault, a minimum displacement of approximately 24 m can be inferred from the geometry of the overlying colluvial wedge (Figure 15d). The topographic profile across the downstream section of stream 2 indicates that T1 presently stands approximately 7 m above stream 2, while the slope break on top of the right river-cut cliff records the initiation of stream incision approximately 12 m above the present channel (Figure 15e). From these observations, the following scenario could be summarized. Before stream 2 began to incise, it was merged with the Kanomljica River at an elevation of approximately 472 m (12 m higher than present). As stream 2 began to incise, the  $53 \pm 5$  m offset began to accumulate. Next, temporary equilibrium was reached in the river channel at the T1 surface elevation where stream 2 flowed into the Kanomljica River. At that time, the right-bank cliff cut by the river NE of the fault reached a height of approximately 5 m (Figure 15e). Next, the Kanomljica channel became narrower and started to incise into T1. Consequently, stream 2 cut downward into T1, which was consequently abandoned, and continued to increase the height of the river-cut cliff. Subsequently, the drainage confluence was pushed

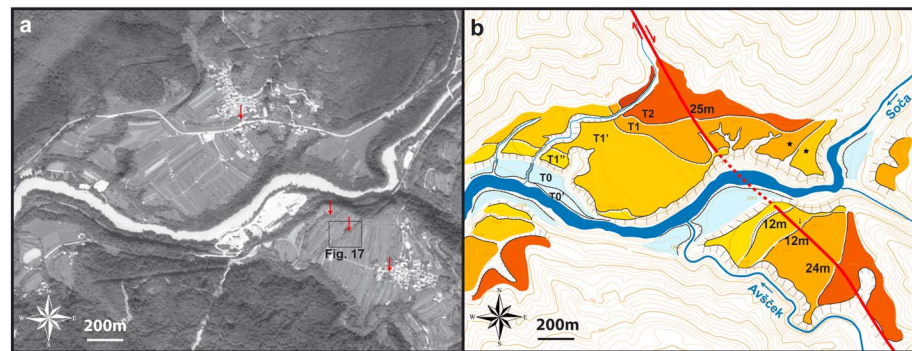


**Figure 16.** (a) A 2.5 m SPOT image and (b) geomorphic interpretation with 1:25,000 topographic map of the Avče site showing the perched alluvial surfaces of the Soča. The red arrows in Figure 16a show the location of the offset terrace risers mapped in Figure 16b. The black stars in Figure 16b show the location of the ditches dug for  $^{36}\text{Cl}$  sampling.

to the NE approximately 50 m from the fault trace, creating the new valley section of stream 2. Therefore, the abandonment of T1 postdates the start of the 53 m offset and predates the 24 m offset.

To identify the age ranges of the offsets, we attempted to date the upper terrace. We dug a pit in T1 (black star in Figure 15a) to collect samples for  $^{36}\text{Cl}$  CRE dating. As anticipated, no alluvial material was found. T1 consists of a bedrock terrace capped by a colluvial wedge (Figure 15f). The colluvial material is uniform throughout its 150 cm thickness and is composed of sparse angular pebbles with diameters of up to 10 cm in a clay matrix. The surface of the bedrock-colluvial transition is wavy but sharp and does not display any evidence of either surface bedrock weathering or paleosol development (Figure 15f). From these observations, we inferred that the deposition of the colluvial wedge occurred shortly after terrace abandonment since the time to develop soils in such wet climate is probably very short. However, we acknowledge that the age of T1 only provides a maximum age for the 24 m offset (production of  $^{36}\text{Cl}$  would have been higher during a hypothetical first phase where T1 would have been directly exposed (not capped by the colluvium) at the surface), although the difference should be quite small. Two samples were collected at the top of the bedrock at depths of 155 and 135 cm, and the [ $^{36}\text{Cl}$ ] results are  $8.73 \cdot 10^4$  and  $9.66 \cdot 10^4$  atoms/g of sample, respectively (Table 1). Assuming a colluvium density of  $2.1 \pm 0.2 \text{ g/cm}^3$  and no erosion and inheritance, the calculated CRE ages are  $14.2 \pm 1.9$  and  $12.7 \pm 2.1$  ka (Figure 15f and Table 1). The two bedrock pieces sampled at approximately the same depth could not be used to accurately assess the denudation rate and inheritance. However, the geomorphic observations clearly suggest that the Kanomljica River is strongly incising into its valley floor, resulting in its narrow and deep valley. Therefore, we speculate that the  $^{36}\text{Cl}$  content in the bedrock before abandonment of the cut terraces was relatively low. On the other hand, our observations suggest that the erosion before the colluvial deposit was probably insignificant. However, the colluvium itself could have been partly eroded. If this is the case, the samples were initially deeper, and the  $12.7 \pm 1.3$  ka ages should be considered as minimum estimates. Therefore, the abandonment of the T1 terrace is probably older than the oldest dated sample, making it older than  $14.2 \pm 1.9$  ka. The meaning of these ages in terms of slip rate assessment will be discussed together with other dates in section 5.1.

### 4.3. Cumulative Offsets Along the Predjama Fault and the Age Constraints of the Smallest Offsets Using $^{36}\text{Cl}$ Depth Profiles

#### 4.3.1. Postglacial Offsets Observed on Soča Terrace Risers Near Avče

Along the Soča River stretch, which has recorded kilometeric displacement along the Predjama fault (section 3.3.1), the river meanders across broad alluvial surfaces, preserved upstream and downstream of the fault (Figures 6b, 16a, and 16b; the area of Figure 16 is shown in Figure 5a). These surfaces presently correspond to cultivated fields on well-developed soils and therefore have smoothed topography (Figure 16a). Figure 16 b shows a detailed map of those surfaces, which are made of unconsolidated ~10–20 m thick conglomerate and cap the Upper Cretaceous flysch deposits. These surfaces correspond to terraces that were emplaced and then incised by the Soča and can be divided into different levels according to their elevation (T0 and T0': modern flood plain; T1, T1', and T1'': sublevels standing between 50 and 70 m; and T2: upper level only preserved in the most sheltered areas) (Figure 16b). Detailed mapping reveals laterally displaced terrace risers.

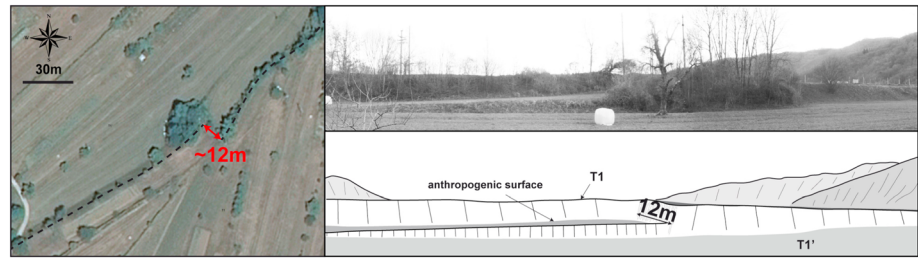


**Figure 17.** (left) A 50 cm orthophoto of the displaced T1'/T1 riser SE of the Soča River. The black dashed line follows the path of the riser, which is also shown by the line of trees. (right) Field photograph of the displaced T1'/T1 riser looking toward the SE from the T1' surface (top) and corresponding sketch (bottom).

The clearest offset is observed on the ~4 m high T1'/T1 riser, which appears right-laterally displaced by  $12 \pm 2$  m (Figure 17). The T1''/T1' riser also displays a sharp shift of approximately 12 m in the continuation of the T1'/T1 riser offset (site of offset is shown with a red arrow in Figure 16), but the presence of a small anthropogenic terrace built below the T1''/T1' riser downstream of the fault (see the dotted line in Figure 16b) suggests that its geometry could have been substantially modified, making an accurate estimation difficult. Larger horizontal offsets of approximately 25 m are also observed on the T1/T2 riser on both sides of the river (sites of offsets are shown with red arrows in Figure 16). Unfortunately, a road and houses have been built near the fault trace, and the poorly preserved riser morphology makes measurements uncertain. Finally, no obvious offset affects the lowest and most recent risers (T0/T1'' and T0'/T1' risers south and north of the river, respectively), probably because of recent refreshing due to river erosion and collapse.

To constrain the timing of these offsets, we attempted to determine the ages of terrace emplacement using  $^{36}\text{Cl}$  CRE dating. We dug two 2–3 m deep pits on the surfaces of T1 and T1' on the right bank of the river at places where they appear the most pristine and less man-modified (black stars on Figure 16b). A depth profile for  $^{36}\text{Cl}$  CRE dating was sampled in each pit. The deposits on both terraces are composed of well-rounded cobbles and pebbles with various diameters of up to 50 cm in an organic matter-coated fine-grained (sands and clays) matrix that represents less than 20% of the material. The cobbles and pebbles mainly consist of limestone with some marlstones representative of the lithology of the drained watershed. Moreover, although the initial signs of cementation can be observed, the resulting conglomerate is loosely consolidated. Using the method described in section 4.1.1, the density of the deposit was estimated at  $2.5 \pm 0.2$  g/cm<sup>3</sup>. Both deposits are capped by a Soil layer that appears thicker (~45 cm) in the T1' profile than in the T1 profile (~20 cm). We sampled 13 pebbles with diameters of 5–15 cm from depths of 25 to 190 cm in T1 and 7 pebbles from depths of 55 to 220 cm in T1'. The  $^{36}\text{Cl}$  concentrations varied from  $2.07 \cdot 10^4$  to  $1.13 \cdot 10^5$  atoms/g of sample within T1 and from  $1.51 \cdot 10^4$  to  $1.04 \cdot 10^5$  atoms/g of sample within T1' (Table 1). The calculated apparent CRE ages (assuming no denudation and no inheritance) of each sample are summarized in Table 1.

The modeling results of the T1 profile indicate that the best fits are obtained for an exposure age of  $9.3 \pm 0.2$  ka, a denudation rate of zero, and  $3.15 \times 10^3$  of  $^{36}\text{Cl}$  atoms/g of homogenous inheritance (Figure 18, left) (this age

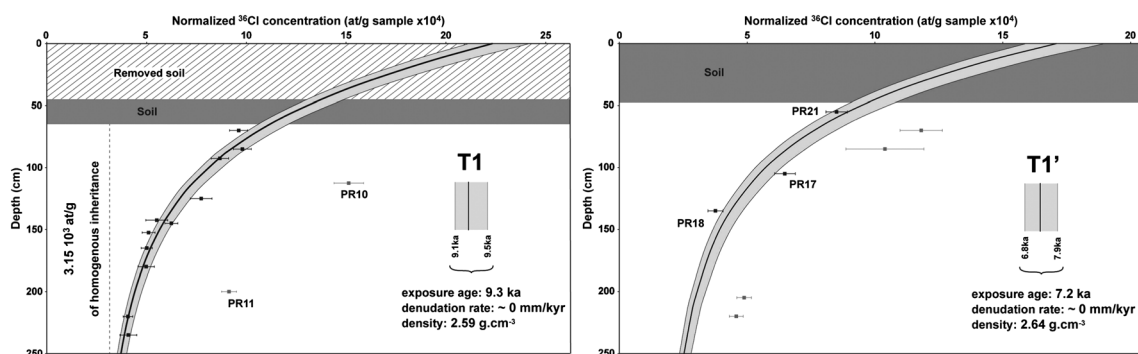


**Figure 18.** Normalized measured  $^{36}\text{Cl}$  concentrations (true concentrations are given in Table 1) as a function of depth along the (left) T1 and (right) T1' terrace profiles (samples excluded from the final model (see the text for explanations) are represented in grey) and the best fit model (black curve).

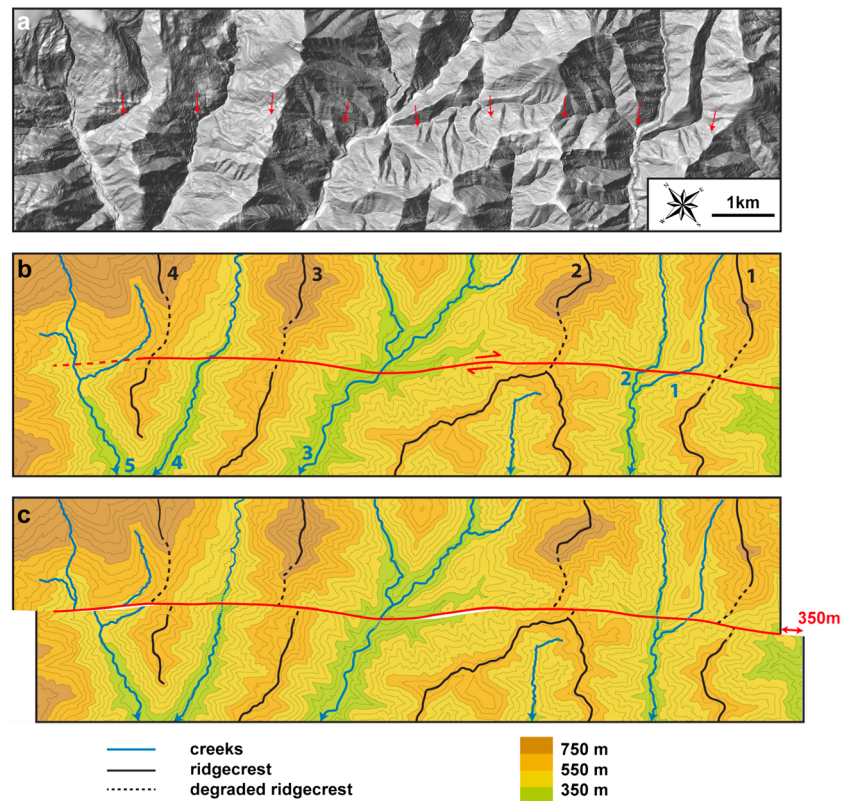


**Figure 19.** (a) Shaded 5 m DEM of the northwestern section of the Predjama Fault in the Veneto Prealps showing surface expressions of faulting (shown by red arrows) and the wrench-shaped courses of the creeks. (b) Topography of the same area with the fault trace, rivers, and ridges mapped in red, blue, and black, respectively. The black dotted lines correspond to sections where the elevations of the ridges decrease, suggesting poor preservation. (c) A 350 m back-slipping of the same fault section. Note the restored continuity of the river courses and large-scale topography of the ridges.

and the associated uncertainty correspond to the weighted mean age and uncertainty calculated from all individual sample ages yielded with a zero denudation rate and  $^{36}\text{Cl}$  atoms/g of inheritance). This modeling result also implies that approximately 45 cm of soil was anthropogenically removed (in agreement with the low soil thickness relative to the T1' profile) (Figure 18, left) and that two samples (PR10 and PR11) accumulated more inheritance than the other 11 samples (see supporting information Text S2 for further explanations). The analysis of the T1' profile suggests that four samples accumulated heterogeneous inheritance relative to the three other samples, which were modeled and yielded the best fits for zero denudation and zero inheritance with an exposure duration of  $7.2 \pm 0.5$  ka (Figure 18, right) (see supporting information Text S2 for further explanation). Thus, the dating results indicate that the  $12 \pm 2$  m displacement recorded by the T1"/T1' riser began to accumulate between  $9.3 \pm 0.2$  and  $7.2 \pm 0.5$  ka. The implications in terms of slip rate assessments will be discussed for other dates in section 5.1.

#### 4.3.2. Systematic Right-Lateral Displacement of Moderate-Sized Drainages Along the Northwestern Section of the Predjama Fault

In the Veneto Prealps, the Predjama Fault strikes N310 and cuts across four adjacent and equivalent intramountain creek catchments before becoming less obvious toward the NW (Figure 2b) and near the Nadiža Valley (Figure 19a). The creeks flow SW, perpendicular to the fault strike, in the bottom of 300–500 m deep V-shaped valleys (Figures 19a and 19b). The fault trace is highlighted by topographic slope breaks and systematic right-lateral shifts in the main creeks (red arrows in Figure 19a). The creek valley floors are 15–60 m wide and appear very linear on both sides of the fault, flowing southwestward except where they intersect the fault. Back-slipping the fault by ~350 m restores the continuity of all of the creeks, thereby providing cumulative displacement (Figure 19c). Although the large-scale trends of ridgecrests 3 and 4 are aligned with this retrodeformation, this is not the case for ridgecrests 1 and 2, possibly because these ridgecrests were significantly degraded across the fault (Figures 19b and 19c).

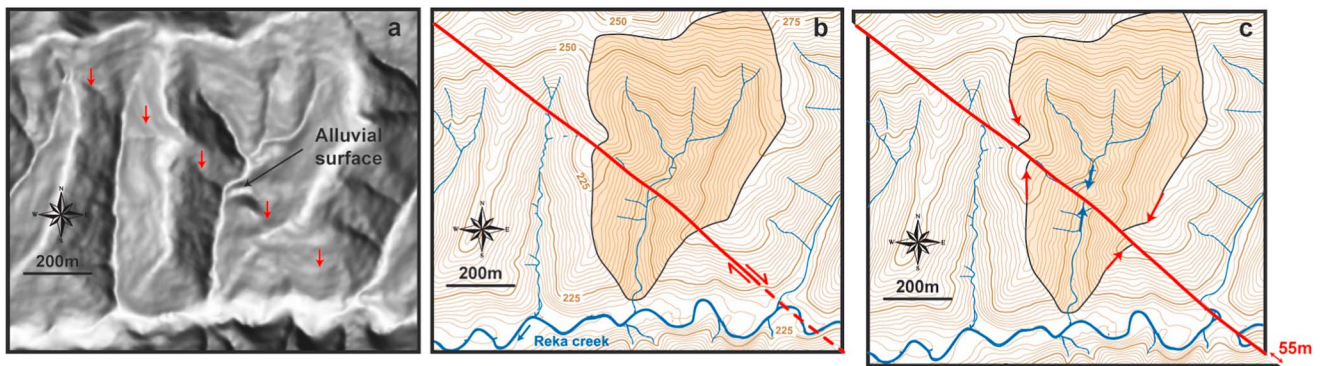


**Figure 20.** (a) Shaded 5 m DEM of the Krasno site showing the wrench-shaped watershed along the Raša Fault (marked by red arrows). (b) Geomorphic interpretation of the same site. The geometry of the watershed is shown in orange. (c) A 55 m back-slip shows the realigned morphologies (ridges with red arrows and river courses with blue arrows).

#### 4.4. Fault Trace Characterization and Cumulative Offsets Along the Raša Fault

Similar to the Predjama Fault, the Raša Fault mainly crosses karstic terrain along its southeasternmost section, preventing the identification of potential markers useful for estimating the recent displacements. To the NW of Gorizia, the fault lies at the front of the Northern Dinarides and crosses NE-SW oriented drainages. In many places, the fluvial activity erased most of the long-term faulting surface expressions during the last deglaciation [Fontana *et al.*, 2008]. However, some fault sections are located a few hundred meters upstream from the range front, where cumulative displacements across drainages of various sizes can be recognized.

##### 4.4.1. The 55 m Offset at the Krasno Site

Because the drainage is mainly NE-SW oriented near the Raša Fault, first-order tributaries, having potentially recorded the most recent motion, rarely cross the fault. We identified one site at Krasno where a first-order catchment is obliquely crossed by the fault (Figures 20a–20c). Cumulative slip on the fault has built a nearly continuous slope break that is revealed by shadows on the illuminated DEM (Figure 20a). The catchment geometry shows a twisted shape along the fault, suggesting that its downstream section was dragged toward the NW with increasing right-lateral slip on the fault (Figure 20b). This watershed is drained by a deeply entrenched stream, which also appears right-laterally offset along the fault (Figures 20a and 20b). Upstream from the fault, a small alluvial surface preserved on the left bank appears abruptly stopping along the fault trace (Figure 20b). Back-slipping along the fault by approximately 55 m restores a more symmetrical catchment shape and creates stream continuity over the alluvial surface (Figure 20c).

##### 4.4.2. The 330 m Offset at the Fornalis Site

The Fornalis site is located 4 km SE of Cividale del Friuli (Figure 1). The fault trace is easily visible as a depressed 100 m wide morphological corridor where fault scarps and triangular facets (shaped by small streams in the middle of the fault section) are observed (Figure 21a). NE of the fault, four creeks flow SW in deeply entrenched valleys incised in Paleocene flysch deposits (Figure 2a). The ridgecrests separating these valleys do not continue across the fault and over a 200–300 m long distance such that all of the valley floors merge into a narrow fault-parallel flat surface, especially along creeks 3 and 4 (Figure 21a). Additionally, the course of creek 1 suddenly changes upon reaching the fault, flowing NW and turning around a fault-parallel relief with an elevation of approximately 200 m asl. An 80 m deep SW sloping dry valley starts on the northeastern edge of this relief. Its orientation and location suggest that creek 1 formerly used to flow through it. The catchments upstream from valleys 3 and 4 upstream from the fault appear relatively small compared to the valley downstream of the fault, suggesting that catchments may have been larger in the past.

Drainages 2, 3, and 4 are clearly right-laterally deflected when crossing the fault. The fact that the ridgecrests bounding these valleys are clearly disconnected on both sides of the fault and do not reveal any topographic continuity in between rules out nontectonic hypotheses regarding the origin of the apparent offset. To restore the geometric continuity of the valleys and realign the drainages and ridgecrests, approximately 330 m of retrodeformation is required along the fault (Figure 21b). This back-slipping also realigns the dry valley with the valley of creek 1 NE of the fault, supporting the interpretation of tectonic displacement.

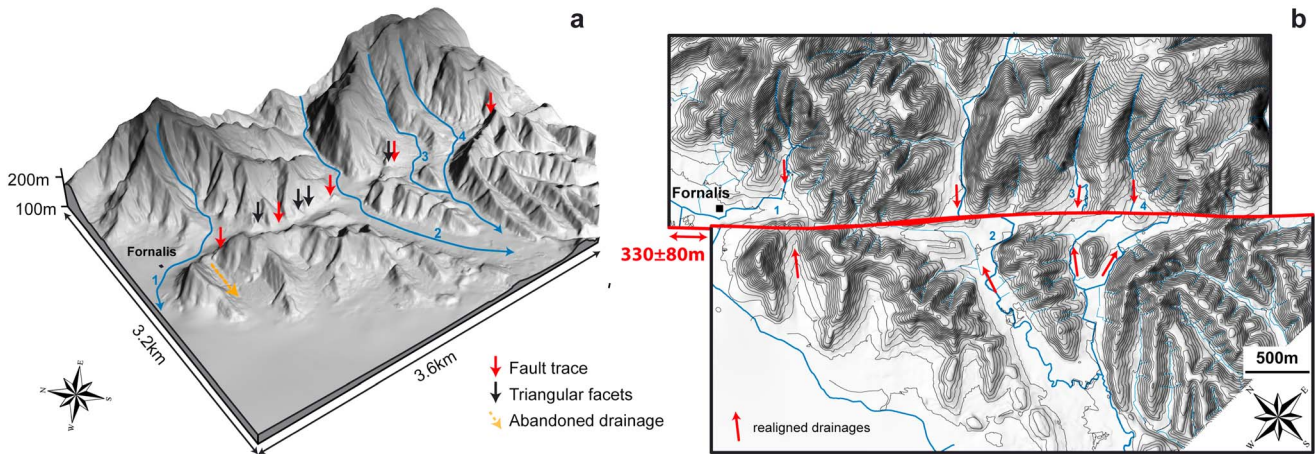


**Figure 21.** (a) A 3-D view of the shaded 5 m DEM of the Fornalis site looking eastward and showing surface expressions of faulting, such as triangular facets along the Raša Fault. Note the deflected river courses and displaced hills on both sides of the fault and the presence of an abandoned drainage SW of the fault. (b) A 330 m back-slipping of the same fault section showing the restored river courses (with red arrows) and hills.

#### 4.4.3. The 175 m Offset at the Campeglio Site

This site is located 5 km NW of Cividale del Friuli at the boundary between the Veneto-Friuli Basin in the SW and the Veneto Prealps (representing the northwestern tip of the Dinarides) in the NE (Figures 2a and 22). In the northeastern half of Figure 22, subvertical beds of sandstones striking approximately N315 control the steep morphology of the relief. The drainages flowing down from the Veneto Prealps are deeply entrenched and separated from each other by prominent ridgecrests before entering the Veneto-Friuli Basin (Figure 22b). In the area of Campeglio, the front of the Dinarides becomes progressively composed of softer flysch sediments (mostly siltstones) and the streams and rivers have gentler morphologies.

The Raša Fault runs across these softer sediments, apparently displacing the ridgecrests (red arrows in Figure 22a) shaped by the Meris and Ellero Creeks near their outlets (Figures 22a and 22b). Along their upstream sections, the two drainages are oriented roughly perpendicularly to the strike of sandstone beds and gently meander on the valley floor. Farther to the SW, they are deflected to the NW when reaching the fault and then follow and laterally erode the base of the relief downstream. In both cases, at the position of the fault, steep NE facing slopes stand just in front of the upstream course and have been clearly right-laterally displaced with respect to their counterparts NE of the fault (Figure 22b).

From these observations, we infer a right-lateral tectonic offset across these hills. Back-slipping the fault section by  $\sim 175$  m restores the continuity and shape of the valleys' morphology (Figure 22c). To the NW, where the exact location of the active trace is less clear, retrodeformation reveals apparent unconformities.

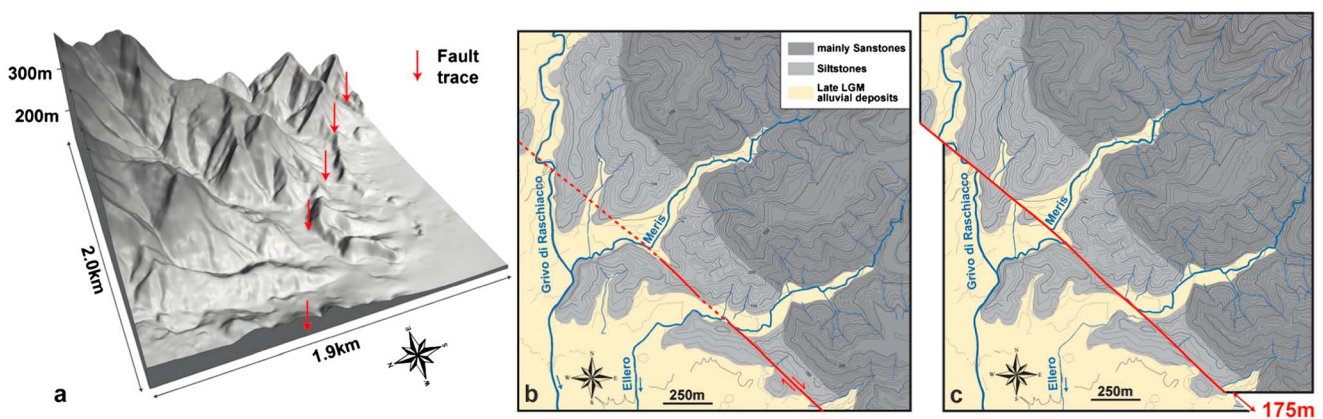


**Figure 22.** (a) A 3-D view of the shaded 5 m DEM of the Campeglio site showing the surface expressions of faulting (red arrows). (b) Geomorphic map of the same area showing the deflected river courses and offset hills along the Raša Fault (drawn in red). (c) A 175 m back-slipping of the same area showing the restored continuity of the relief.

**Table 2.** Summary of the Horizontal Offsets, the CRE, and Estimated Ages (for the Anžic and Pri Fežnarju Sites, the Age Is Assumed to Be Bounded by the CRE Minimum Ages and the Maximum Age Inferred in Section 5.1), and the Deduced Slip Rates Along the Dinaric Faults<sup>a</sup>

Site	Horizontal Offset (m)	Age (ka)	Slip Rate (mm/yr)	Type of Dated Marker
<b>Idrija fault</b>				
Anžic	48 ± 12	14.7 ± 4.4 ( <i>min</i> )	3.8 ± 2.0 ( <i>max</i> )	river-cut cliff
Kapa <sup>b</sup>	42 ± 3	23.5 ± 5.5	1.9 ± 0.6	stream channel
Pri Fežnarju	53 ± 5	14.2 ± 1.9 ( <i>min</i> )	3.3 ± 1.3 ( <i>max</i> )	entrenched channel
Pri Fežnarju	≈24	14.2 ± 1.9 ( <i>max</i> )	1.7 ± 0.2 ( <i>min</i> )	colluvial wedge
Rizevce <sup>b</sup>	38 ± 6	23.5 ± 5.5	1.75 ± 0.65	ridgecrest-abandoned drainage
Godovič	110 ± 20	142.5 ± 13.5	0.8 ± 0.2	entrenched channel
Anžic	135 ± 40	142.5 ± 13.5	1.0 ± 0.4	incised valley
Kapa <sup>b</sup>	140 ± 70	142.5 ± 13.5	1.0 ± 0.6	ridgecrest-creek course
Kapa <sup>b</sup>	360 ± 20	257.5 ± 22.5	1.4 ± 0.2	paleovalley
Dolenja Trebuša	2500 ± 500	3000 ± 500		paleovalley, incised valleys
<b>Predjama fault</b>				
Avče	12 ± 2	8.15 ± 1.35	1.6 ± 0.5	ridgecrest-stream channels
Veneto Prealps	350 ± 40	257.5 ± 22.5	1.4 ± 0.3	creek courses
Čepovan	500 ± 50 <sup>c</sup>	800 ± 400		abandoned canyon cliffs
Avče	960 ± 210	800 ± 400		ridgecrest-river course
<b>Raša fault</b>				
Krasno	55 ± 15	23.5 ± 5.5	2.65 ± 1.25	ridgecrests-stream channel
Campeglio	175 ± 20	142.5 ± 13.5	1.25 ± 0.25	ridgecrests-creek valleys
Fornalis	330 ± 80	257.5 ± 22.5	1.3 ± 0.4	ridgecrests-creek valleys

<sup>a</sup>Ages associated with the largest displacements were inferred by assuming constant slip rates (section 5.1). The three offsets associated with <sup>36</sup>Cl CRE ages are in italics.

<sup>b</sup>Data were obtained from *Moulin et al.* [2014].

<sup>c</sup>Distributed motion on the two branches of the Predjama Fault.

The Grivo di Raschiacco Valley continuity is lost, probably because this river formerly flowed more to the NW, where it deposited a large alluvial fan (Figures 22c and 2b). Between this river and the Meris Creek, a first-order stream stands in front of a bedrock ridge. This stream drains a catchment that is smaller than the Meris and Ellero catchments, suggesting that it acquired its present geometry more recently, which explains its inconsistent location in Figure 22c.

## 5. Discussion

### 5.1. Ages of the Offset Landforms and Late Pleistocene Rates of Slip Along the Dinaric Faults

In section 4, 10 cumulative right-lateral offsets, as well as 4 additional offsets along the Idrija Fault from *Moulin et al.* [2014], ranging from 12 ± 2 to 360 ± 20 m, have been quantified from 17 geomorphic markers (Table 2). At three sites <sup>36</sup>Cl-dating of displaced markers have been performed and allow placing bounds on the rates of slip along the Idrija and Predjama Faults. At the Anžic site, dating results indicate a minimum age of 14.7 ± 4.4 ka for the 48 ± 12 m offset, thus yielding a maximum slip rate of 3.8 ± 2.0 mm/yr for the Idrija Fault (Table 2). At Pri Fežnarju, the 14.2 ± 1.9 ka age deduced for the abandonment of the T1 terrace provides a maximum age for the 24 m displacement recorded by the colluvial wedge and a minimum age for the 53 ± 5 m displacement recorded by stream 2. A slip rate between 1.7 ± 0.2 and 3.3 ± 1.3 mm/yr could thus be inferred for the Idrija Fault at this site (Table 2), in agreement with the maximum slip rate deduced at Anžic. At the Avče site, ages of 9.3 ± 0.2 and 7.2 ± 0.5 ka have been determined for the abandonment of the T1 and T1' terraces indicating that the Predjama Fault slip rate is 1.6 ± 0.5 mm/yr at this site (Table 2).

Those constraints on the rates of slip now allow discussing the ages of the other displacements. Because all have been quantified from the geometry of entrenched rivers and valleys, the amounts of cumulative offsets have been first plotted against the drainage area of the catchments upstream of each offset (Figure 23). Except for three points, a good correlation is observed between three relatively well-defined groups, and their cumulative offsets increase as the catchment surface area increases. The three data points that are not correlated correspond to the offsets measured from the drainages at the Fornalis site and along the Predjama Fault, which are potentially associated with larger catchment areas than today (section 4.4.2). The correlation observed with all the other recorded offsets agrees with the idea that the rate of catchment

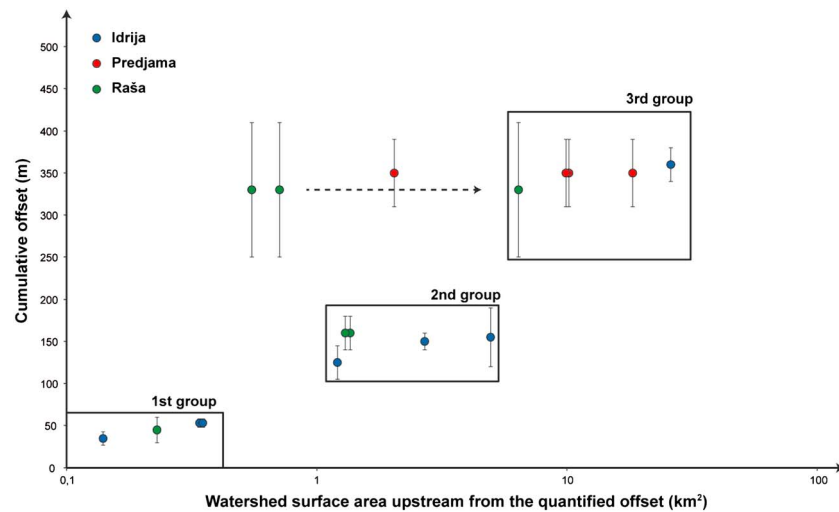


**Figure 23.** Cumulative offsets plotted versus the drained surface upstream of the fault. In cases where drainages or associated markers recorded several cumulative offsets, only the largest one was considered. The black dotted arrow represents the plausible shift in the three outliers because of decreases in the catchment sizes (see in the text for explanation).

growth is time dependent [e.g., Bull, 2008]. Thus, the streams with small catchment areas either developed too recently to have recorded the long periods of displacement or their stream power was too low to sufficiently incise and maintain their course [e.g., Hubert-Ferrari et al., 2002].

Catchment growth is mainly controlled by capture processes, which are promoted by enhanced stream power [Bull, 2008]. Therefore, one could assume that catchment growth has mainly occurred during events of enhanced incision. This suggests that the three groups observed in Figure 23 correspond to three major incision events and thus that all offsets within each group are coeval. For the first group this inference is independently supported by the fact that (1) minimum ages for those offsets, as determined by  $^{36}\text{Cl}$  dating, are very similar at the Pri Fežnarju and Anzic sites (Table 2), and (2) the smallest offsets quantified along the Idrija Fault have been recorded by similar markers, that is, on first-order tributaries with typical lengths of 1 km, thus suggesting that they formed roughly synchronously. The  $53 \pm 5$  m offset quantified at Pri Fežnarju belongs to the first group. While the minimum age of this offset is  $14.2 \pm 1.9$  ka, the upper bound could be estimated from the minimum slip rate of  $1.7 \pm 0.2$  mm/yr determined at this site. It yields a maximum age of 38.7 ka.

The 14.2–38.7 ka time range roughly corresponds to the last glacial maximum, a period when changes in the modes of erosion is likely to have controlled the preservation of tectonic offsets [e.g., Peltzer et al., 1988; Winter et al., 1993]. Due to the presence of the former neighboring ice sheets (Figure 2b), the studied sites, at elevations of 400 masl on average, were likely subjected to periglacial conditions during the last glacial phase. In this context, earlier cumulative offsets and fault scarps were potentially erased due to erosional processes [e.g., Peltzer et al., 1988; Winter et al., 1993]. Because incision events along such small tributaries are mainly controlled by local climatic conditions [e.g., Merritts et al., 1994], it could be speculated that the erosion became mainly confined along the channels along with the drastic climate changes that occurred during the last deglaciation [e.g., Peltzer et al., 1988; Winter et al., 1993]. This scenario of offsets preservation accounts for both the 14.2–38.7 ka time range which has been independently deduced and the regional signal suggested by the grouping of offsets values (Figure 23).

The assumption that deglaciation phases controlled the preservation of tectonic displacements could be tested by considering that the three groups of Figure 23 are associated to the last three deglaciations. That would mean that large and well-incised drainages might be stable enough to continuously record slip along faults, even across glacial periods [e.g., Peltzer et al., 1988; Winter et al., 1993]. The LGM chronology is particularly well established in the Friuli area. The glacial pulses of the Tagliamento Glacier (see Figure 1 for location) have been constrained by several authors [Avigliano et al., 2000; Monegato et al., 2007; Paiero and Monegato, 2003; Vaia, 1982] and summarized by Monegato et al. [2007]. These data suggest that the

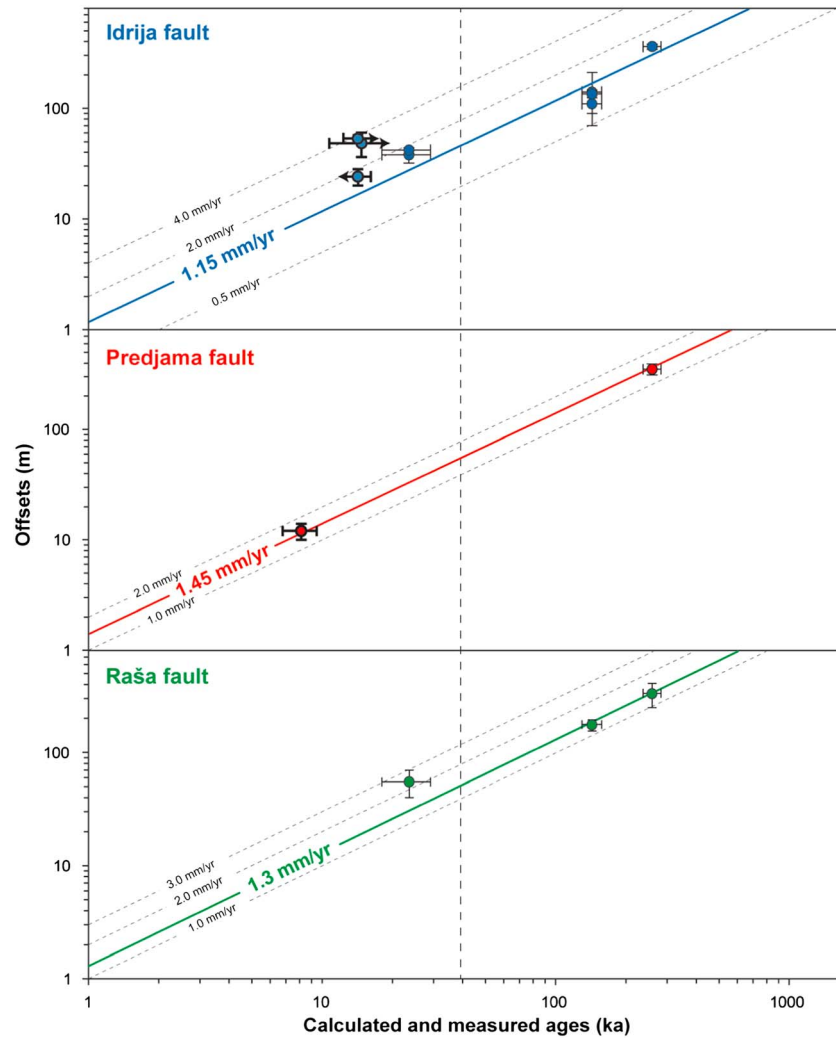


**Figure 24.** Slip rate assessments along the three Dinaric faults from offset measurements and CRE and assessed ages. Data points with thick and thin black lines refer to offsets of  $^{36}\text{Cl}$ -determined ages (arrow to right when determined ages are minimum and arrow to left when determined ages are maximum) and estimated ages (correlated to former glaciations). Thick lines show the weighted mean slip rates obtained from each data set. The vertical dashed line represents the maximum age (38.7 ka) supported by the smallest offsets (see further explanations in the text).

maximum glacial advance was reached between 29 and 24.5 ka, followed by a short phase of retreat up to 22 ka and a cold period that triggered a final glacial advance between 22 and 21 ka. Between 21 and 18 ka, the ice sheet retreated dramatically. Then the timing of the local LGM is  $23.5 \pm 5.5$  ka. At global scale the last three glacial maxima could be placed at  $21.0 \pm 3.0$  ka,  $140 \pm 11$  ka, and  $255 \pm 20$  ka when using the stack curve of benthic  $\delta^{18}\text{O}$  as a record of the global glacial chronology [Lisiecki and Raymo, 2005]. We incorporated the uncertainty associated to the comparison between local and global LGM into the timing of former glaciation and thus attributed ages of  $23.5 \pm 5.5$  ka,  $142.5 \pm 13.5$  ka, and  $257.5 \pm 22.5$  ka for the three groups of offsets, respectively. All cumulative displacements associated to their determined or estimated ages are plotted in Figure 24.

The assumption that former deglaciations have controlled the preservation of cumulative displacements is supported by the good consistency between measured and estimated slip rates along the Predjama Fault, suggesting a mean slip rate of  $1.45 \pm 0.25$  mm/yr (Figure 24). Measured and estimated ages of the cumulative offsets along the Idrija and Raša Faults also support this, although a constant slip rate is supported by the smallest offsets only if considering the very lower bounds of the calculated slip rates (Figure 24). When averaged over the last 255 ka, mean slip rates of  $1.15 \pm 0.15$ ,  $1.45 \pm 0.25$ , and  $1.30 \pm 0.20$  mm/yr are yielded along the Idrija, Predjama, and Raša Faults, respectively (Figure 24).

Given the uncertainties associated to all measurements, it is difficult to decide if the slight increase in slip rate along the Idrija and Raša Faults is a true feature (Figure 24). It has been shown that the maximum age supported by the smallest displacements is 38.7 ka. If considering this value (indicated with a vertical dashed line in Figure 24), there is no more detectable increase in slip rates over the most recent period. Therefore, a possibility could be that the preservation of the smallest offsets occurred slightly before the LGM, although all other data strongly support the idea that former deglaciations have controlled the timing of offsets accumulation. Conversely, if the increase in slip rate is a true feature, then two main possibilities could be proposed to account for this observation.

Along the central section of the Idrija Fault the amount of (assumed coeval) slip apparently varies from one site to the other (see for more details *Moulin et al.* [2014]):  $42 \pm 3$  m at the Kapa site (4 km NW of Idrija),  $53 \pm 5$  m at the Pri Fežnarju site (8 km NW of Idrija), and  $38 \pm 6$  m at the Rizevce site (13 km NW of Idrija) (Table 2). These variations could reflect the decrease in the amount of slip toward the tips of the fault segments during individual earthquakes [e.g., *Davis et al.*, 2005; *Manighetti et al.*, 2001; *Manighetti et al.*, 2005; *Nicol et al.*, 2005; *Rockwell and Klinger*, 2013; *Scholz*, 2002]. The apparent maximum offset would occur at the Pri Fežnarju site, with a total of approximately  $53 \pm 5$  m, while cumulative offsets along the sections of smaller displacement would not have been preserved. Assuming that the displacement is greatest at Pri Fežnarju and decreases to zero at the fault tips, the mean displacement would be approximately 25–30 m, which would yield a slip rate of approximately  $1.6 \pm 0.7$  mm/yr. This value agrees better with the averaged slip rate over the last 255 ka, suggesting that sampling of longer-term offsets would not have been biased by this slip variability along the strike. Along the Raša Fault, the  $55 \pm 15$  m offset quantified at Krasno could be similarly considered as the maximum displacement, and the value of the mean slip rate would be closer to the mean slip rate over the last 255 ka when the same rationale is applied.

The second possibility lies in the proposition that the rates of slip along an individual fault can vary with time over cycles of up to several tens of thousands of years [e.g., *Rockwell et al.*, 2000; *Scholz*, 2010; *Benedetti et al.*, 2013]. If real, the apparent postglacial increases in the slip rates of the Dinaric Faults would agree with similar observations from comparisons between Holocene and longer-term fault slip rates at the global scale [*Nicol et al.*, 2009]. The observed differences are possibly related to incomplete capture of the seismic cycle [*Nicol et al.*, 2009] or the modulation of the rates by loading effects induced by surface loads changes [e.g., *Hetzl and Hampel*, 2005].

Consequently, the slip rate averaged over the last 255 ka along the Dinaric faults is probably the most representative of the mean slip rate because it smooths any potential slip variability along the strike and with time. If we consider only the displacements that we have correlated with the  $142.5 \pm 13.5$  and  $257.5 \pm 22.5$  ka deglaciations, the weighted mean slip rates are  $1.1 \pm 0.1$  mm/yr,  $1.4 \pm 0.3$  mm/yr, and  $1.25 \pm 0.20$  mm/yr for the Idrija, Predjama, and Raša Faults, respectively, accounting for  $3.75 \pm 0.6$  mm/yr of the right-lateral slip along the DFS during that period.

## 5.2. Plio-Pleistocene Faulting History and Evidence for Sequential Fault Activation

We can discuss the onset of faulting if we assume that the 255 ka averaged slip rates remained constant over longer periods. The inception of the Idrija Fault would have occurred at  $4.3 \pm 0.4$  Ma, which is during the early Pliocene. This age agrees with the major kinematic changes that occurred throughout the Eastern Alps-Carpathians-Pannonian Basin system at that time [e.g., *Vrabec and Fodor*, 2006]. The Miocene E-W extension that is widely observed in the Eastern Alps and Pannonian Basin would have stopped in the Early Pliocene due to the locking of the Carpathian subduction zone [*Bada et al.*, 2007; *Csontos et al.*, 1992; *Horváth*, 1995; *Peresson and Decker*, 1997; *Ratschbacher et al.*, 1991; *Royden*, 1993]. It is possible that the stretching of the Pannonian lithosphere controlled its fragmentation and the onset of the rotation of Adria along the Idrija Fault, which began to act as a new lithospheric boundary [*Márton et al.*, 2003].

In the study area, the Neogene evolution could be summarized as follows. During the Miocene, the Northern Dinarides were bounded in the north by the active front of the Southern Alps [e.g., *Placer et al.*, 2010] (see also Figure 2a and inset of Figure 2a). At that time, the Dinaric faults were probably activated as normal faults that accommodated the E-W stretching of the Pannonian lithosphere [*Žibret*, 2015] (note that the comparison between geomorphic and geological slip vectors would imply that such extension accounted for a very small amount of slip compared to the subsequent strike-slip phase (section 3.5 and

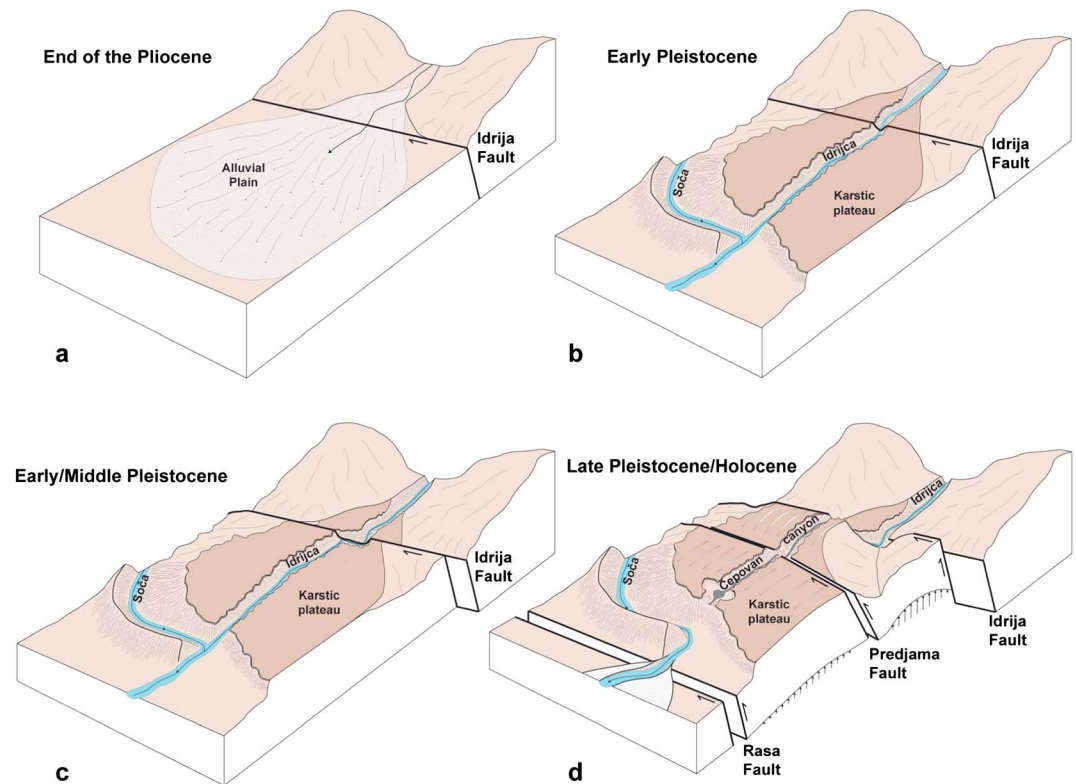


**Figure 25.** Three-dimensional sketches looking northward and summarizing the plausible sequential fault activation and related vertical deformations during the Pleistocene near the Čepovan Canyon. (a) Pure strike-slip faulting along the Idrija Fault and deposition of a large alluvial fan in the SW. (b) Pure strike-slip faulting along the Idrija Fault, deepening of the Čepovan Canyon and the Soča Valley within the old alluvial fan, and karstification of the plateau with limestone outcrops in response to a change in climate. (c) Approximately half of the 2.5 km offset along the Idrija Fault resulted from accumulation. (d) Activation of the Predjama and Raša Faults and onset of the vertical deformation (vertical motions on faults and folding). Note that the timing of inception of slip along the Raša and Predjama Faults is only indicative. Id.F = Idrija Fault; Pr.F = Predjama Fault; and Ra.F = Raša Fault.

supporting information Text S1)). Thus, the kinematic change observed in the Early Pliocene would correspond to more localized deformation along the Northern Dinarides from there acting as a lithospheric boundary between the Adria microplate and the Pannonian Basin. Therefore, the inception of right-lateral motion at the northeastern boundary of modern Adria could be considered as a local expression of the fragmentation of the Adriatic promontory [e.g., D'Agostino *et al.*, 2008; Oldow *et al.*, 2002].

The comparison between long-term geomorphically derived and geologically derived slip vectors suggests that the kinematics was mainly strike slip during the first phase of slip along the Idrija Fault (section 3.5 and supporting information Text S1). At a certain time of that period, the Idrija Fault was bounded by a wide alluvial plain to the SW (Figure 25a). This alluvial plain was then karstified (the karstic surface now preserved on some parts of the Trnovski Gozd plateau) and incised by the main rivers of the area to carve the deeply entrenched valleys, which are presently observed, as well as the Čepovan canyon (Figure 25b). Resolving the timing of that incision event by assuming constant slip rate along the Idrija Fault (that is similar to the one determined over the last 255 ka) yields an age of  $2.3 \pm 0.7$  Ma (near the Plio-Pleistocene boundary). This inference supports the idea that the major drainages of the area began to deepen (and the Trnovski Gozd plateau started to karstify) in response to the climate forcing associated with the Plio-Pleistocene transition [Habič, 1968] (Figure 25b) between 2.5 and 3.5 Ma [e.g., Miller *et al.*, 2005]. From that time the Čepovan canyon began to accumulate right-lateral displacement along the Idrija Fault (Figures 25b and 25c).

On the other hand, while the late Pleistocene slip rates of the Idrija and Predjama Faults appear similar, the cumulative displacement of the Soča Valley strongly differs between the faults ( $2.5 \pm 0.5$  km and  $960 \pm 210$  m, respectively). Moreover, the geological offset along the Predjama Fault matches, within uncertainties, the

$960 \pm 210$  m long-term geomorphic displacement. This suggests that the Soča Valley captured the entire slip along the Predjama Fault. The reconstruction of Figures 25a and 25b indicates that the onset of slip along the Predjama Faults (fully recorded by the displacement of the Soča River) occurred not earlier than  $\sim 2.5$  Ma. Conversely, if a constant slip rate is assumed along the Predjama Fault (that is similar to the one determined over the last 255 ka), the onset of faulting could be as young as  $750 \pm 310$  ka, in the early middle Pleistocene. The topography of the Čepovan canyon also revealed a significant vertical component (including folding) of the deformation across the DFS (section 3.4) (Figure 25d). The vertical displacement along the Idrija Fault is apparently similar when determined from the Čepovan canyon topography (section 3.4) or from geological data (supporting information, Text S1) suggesting that the inception of vertical displacement also occurred not earlier than  $\sim 2.5$  Ma. Those inferences strongly suggest that the activation of the Predjama Fault and the onset of uplift were coeval (Figure 25d), in agreement with Figure 10, which suggests a major role of the Predjama Fault in accommodating the folding of the Čepovan canyon.

We already noted that overdeepening is not observed across the Čepovan canyon in the vicinity of the fold hinge suggesting that folding occurred after the abandonment of the canyon (section 3.4.2). It follows that the 300 m depth of the canyon has been carved between 2.5 Ma (according to the reconstruction of Figure 25b) and the time of activation of the Predjama fault, suggesting that this later occurred quite long after 2.5 Ma. In the absence of additional information about changing slip rates along those faults we retain the  $750 \pm 310$  ka age as an indication of the timing of this kinematic change (Figure 25c). Finally, the similarities between the late Pleistocene slip rates and the total geological displacements recorded along the Raša Fault suggest that this fault was activated at approximately the same time (Figure 25d).

Unless balanced by coeval changes on unrecognized nearby faults, what we believe to be unlikely, the onset of faulting along the Predjama and Raša Faults at  $750 \pm 310$  ka implies a drastic kinematic change because it suggests an increase from 1 to approximately 3 mm/yr of cumulative right-lateral motion. Moreover, the transition from pure strike slip to transpressive kinematics is also supported by the drainage patterns reconstructed for the Pliocene: the existence of the wide alluvial plain SW of the Idrija Fault (i.e., the former Trnovski Gozd plateau) suggests that this area was either subsiding or vertically stable; therefore, the recent uplift was caused by a switch in the direction of motion. Overall, our results suggest that the size and orientation of the vector describing the motion accommodated across the DFS changed significantly approximately 750 ka ago.

During the same period, dramatic kinematic changes occurred in the southern parts of the circum-Adriatic region, such as in the Calabrian arc in southern Italy [Mattei *et al.*, 2007] and the central [Galadini, 1999] and southern Apennines [Hippolyte *et al.*, 1994]. This study provides evidence of roughly coeval change in the northern Adriatic sector, suggesting that the early-middle Pleistocene transition could have been a time of major tectonic change that possibly affected the entire Adriatic domain. Our findings represent new quantitative data that can be used to better understand how these changes could be related to the approximately synchronous tectonic transitions observed across the entire Eastern Mediterranean [Schattner, 2010] and the post-3.16 Ma change in the Nubia-Eurasia plate motion [Calais *et al.*, 2003].

### 5.3. Kinematics of the DFS and Their Significance in the Circum-Adriatic Block Tectonic Framework

Our results suggest that  $3.8 \pm 0.6$  mm/yr of right-lateral motion with a  $N312 \pm 3$  trend is accommodated along the Northern Dinarides. In addition to this main horizontal component, a strike-perpendicular shortening has been inferred from folding geometry of the Čepovan Canyon. The  $440 \pm 70$  m of shortening recorded by the canyon probably began accumulating at  $750 \pm 310$  ka. Because no evidence indicates a more recent kinematic change, we speculate that this strike-perpendicular component is still active. Accordingly, a shortening rate of  $0.75 \pm 0.4$  mm/yr is estimated based on the estimated age and quantified shortening. The sum of the strike-parallel and strike-perpendicular components can be used to calculate the slip vector for the studied part of the Northern Dinarides. This calculation is represented in Figure 26 and corresponds to a value of  $3.8 \pm 0.6$  mm/yr with a direction of  $N323 \pm 9$ . Only two permanent GPS stations, located in Ljubljana and 6 km east of Trieste, allow for a comparison of this vector with geodetic measurements. The two stations suggest right-lateral motion along a  $N310 \pm 19$  direction at a rate of  $2.6 \pm 2.0$  mm/yr [Caporali *et al.*, 2008]. Although reliably describing the present deformation would require a greater number of stations, the slip vector determined by the present study agrees with the available geodetic data (Figure 26).

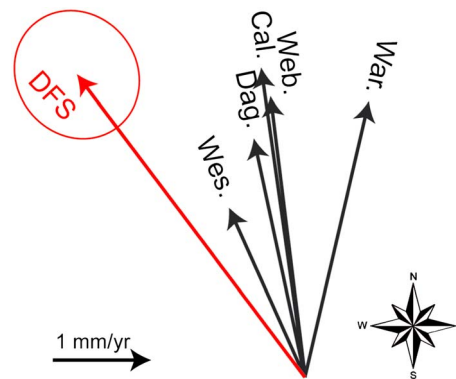


**Figure 26.** Comparison of the constrained slip vector across the DFS (in red) and the motion of Adria with respect to stable Europe predicted by various models at the western front of the DFS (in black) (Wes. = Westaway [1990]; Dag. = D'Agostino et al. [2008]; Cal. = Calais et al. [2002]; Web. = Weber et al. [2010]; and War. = Ward [1994]).

Based on the large-scale geometry and kinematics of studied faults and geological data, we suggest that the motion is localized along a deep structure at depth (section 3.5), which we propose to match the geophysical discontinuity interpreted from interpreted 2-D seismic data acquired along the Alp07 profile Šumanovac et al. [2009]. Based on this geophysical profile, which is crossing the Dinarides at a right angle at the latitude of Rijeka (located along the eastern Adriatic coast, 15 km south of the limit of Figure 1), with support of gravity modeling, Šumanovac et al. [2009] proposed that the Dinarides fold-thrust belt is bounded on both

sides by two major faults that dip steeply to the NE and extend across the entire 15 km of the upper crust. In our interpretation, these crustal-scale faults could correspond with the Idrija and the Raša Faults. Deeper in the crust, these faults possibly merge into a single major discontinuity that displaces the Moho. Šumanovac et al. [2009] suggest that this feature indicates the eastward subduction of the Adriatic mantle [see Brückl et al., 2010]. This major boundary probably corresponds with the deep root of the Idrija Fault. In this case, the DFS represents the northeastern boundary of the Adria microplate and accommodates a part of its counterclockwise rotation through transpressive right-lateral motion along the  $N323 \pm 9$  direction.

The counterclockwise rotation of the Adria microplate is thought to represent the most important driving mechanism of active deformations in the circum-Adriatic region [e.g., Anderson and Jackson, 1987; D'Agostino et al., 2008; McKenzie, 1972; Nocquet, 2012]. Different poles of rotation and velocities have been determined, and all solutions converge to a counterclockwise rotation ranging from 0.25 to 0.52°/Ma around a pole located in the Western Alps or in the western part of the Po Plain [Calais et al., 2002; D'Agostino et al., 2008; Ward, 1994; Weber et al., 2010; Westaway, 1990]. Using these parameters, we plotted the model slip vector predicted by the motion of Adria with respect to stable Eurasia at the front of the Dinarides (near Gorizia) (Figure 26). Regardless of the chosen pole of rotation, all model slip vectors show a consistent NNW to NNE motion, with a velocity ranging from 1.9 to 3.2 mm/yr. These values are all within the range of slip vector across the Northern Dinarides determined in this study and agree with the hypothesis that right-lateral strike-slip faults in the Northern Dinarides accommodate a substantial portion of the Adria motion relative to stable Eurasia. However, while the N-S component of the DFS vector appears remarkably consistent with the models, an E-W component is lacking for matching the observed and predicted slip vectors.

Thus, the additional E-W oriented shortening component could have been neglected in the vector calculation. To account for the predicted Adria/Eurasia displacement, this shortening component should be oriented approximately E-W and have a magnitude of 1–2 mm/yr, which is roughly within the same range as the shortening component across the Friuli Belt [D'Agostino et al., 2005; Grenerczy et al., 2005]. Part of this strike-perpendicular component is probably absorbed across the Kras plateau, which forms a SE-NW oriented 15 km wide anticline located between the Raša Fault and the Adriatic Sea shore (Figure 1). There is no estimation of the shortening absorbed across this structure. However, the modest ~400 m elevation of the anticline (with respect to the Friuli anticlines, for example) suggests that active shortening should be significantly less than 1–2 mm/yr. From the observed discrepancy between predicted and observed vectors (Figure 26), we then infer that Adria does not directly interact with stable Eurasia along the Northern Dinarides. This implies that some part of the stress imposed by the Adria rotation is transferred farther to the east [Cheloni et al., 2014; Grenerczy et al., 2005] and that the DFS should represent the boundary between Adria and another independent block or microplate farther to the east [Márton et al., 2002; Picha, 2002; Tomljenović and Sontos, 2001].

## 6. Conclusions

Using satellite and aerial images, accurate DEMs, topographic maps, and field investigations, we mapped the surface expressions of the three main right-lateral Dinaric faults (Idrija, Predjama, and Raša Faults), which is a prerequisite for quantifying cumulative offsets. At 13 sites, horizontal displacements were measured ranging from 12 m to 4.7 km. At three sites,  $^{36}\text{Cl}$  CRE dating was performed to constrain the ages of the offset markers. Combining chronologically constrained displacements with relative chronologies inferred for the other displacements allowed us to constrain the slip rates of the three Dinaric faults with a maximum uncertainty of 30%. Our results suggest that  $3.8 \pm 0.6$  mm/yr of right-lateral motion, equally shared by the three faults, has been absorbed along the Northern Dinarides over the last 255 ka. Quantifying the total geomorphic and geological displacements along these faults suggests that the Idrija Fault was first activated during the Early Pliocene and that the onset of slip along the Predjama and Raša Faults occurred later, probably closer to the early-middle Pleistocene boundary. In addition to the main horizontal motion, a significant perpendicular strike component has been inferred, which probably began at the same time on the Predjama and Raša Faults and is likely still ongoing. The magnitude of the calculated slip vector describing the motion absorbed across the studied part of the Northern Dinarides agrees with the predicted motion of Adria with respect to stable Eurasia. In addition, the presence of a lithospheric discontinuity to the Moho beneath the Northern Dinarides suggests that the Dinaric fault system could represent the northeastern boundary of the Adria microplate. Finally, significant misfit between the orientations of the predicted and observed vectors may suggest that Adria does not directly interact with the stable Eurasia along this boundary; thus, the motion of the Adria microplate imposes far-field stresses that are transferred farther to the east.

### Acknowledgments

Our work was partly funded by the INSU-CNRS (project entitled SLORISK responsible L. Benedetti). We acknowledge the support of the Slovenian Research Agency (project J6-4016 and program P1-0011). We are grateful to all of the members of the Geological survey of Slovenia (Miloš Bavec, Jernej Jež, Anže Markelj, and Staša Čertalič) for their help and support in the field. Lidar data acquisition was supported by UK NERC. Initial lidar data processing was carried out at the University of Cambridge, Unit for Landscape Modeling and University of Leicester, Department of Geography. In addition, S. Grebby, K. Tansey, and D. Cunningham are acknowledged for this work. The Friuli-Venezia Giulia region is also acknowledged for providing free 1:5000 topographical maps (Irdat.regione.fvg.it/CTRNV). CNES-Toulouse is also acknowledged for providing the SPOT satellite images through the ISIS program dedicated to the scientific community. We are very thankful to J. Marin and all of the staff at SARM-CRPG (France) for performing the chemical measurements. The ASTER French AMS national facility (CEREGE, Aix-en-Provence) is supported by the INSU-CNRS, the French Ministry of Research and Higher Education, IRD, and CEA. We acknowledge B. Sadier for helping us process the lidar data and Jim Tesson and Julie Pupier for their help in the field. We also gratefully acknowledge Irena Mrak and Vincent Godard for their fruitful discussions on the morphogenesis of karst plateaus and river profile analysis, respectively. Readers are welcome to contact the corresponding author (moulin@cerge.fr or adridri777@gmail.com) for any inquiry regarding the present study and data access.

### References

- Anderson, H., and J. Jackson (1987), Active tectonics of the Adriatic region, *Geophys. J. Int.*, *91*(3), 937–983.
- Anzidei, M., P. Baldi, G. Casula, A. Galvani, E. Mantovani, A. Pesci, F. Riguzzi, and E. Serpelloni (2001), Insights into present-day crustal motion in the central Mediterranean area from GPS surveys, *Geophys. J. Int.*, *146*(1), 98–110.
- Aoudia, A., A. Saraò, B. Bukchin, and P. Suhadolc (2000), The 1976 Friuli (NE Italy) thrust faulting earthquake: A reappraisal 23 years later, *Geophys. Res. Lett.*, *27*(4), 573–576, doi:10.1029/1999GL01071.
- Avigliano, R., G. di Anastasio, S. Improta, M. Peresani, and C. Ravazzi (2000), A new late glacial–early Holocene paleobotanical and archeological record in the Venetian Pre-Alps: The peat-bog of Palughetto (Cansiglio Plateau), *J. Quat. Sci.*, *15*(8), 789–803.
- Bada, G., F. Horváth, P. Dövényi, P. Szafán, G. Windhoffer, and S. Cloetingh (2007), Present-day stress field and tectonic inversion in the Pannonian basin, *Global Planet. Change*, *58*(1), 165–180.
- Bavec, M., S. M. Tulaczyk, S. A. Mahan, and G. M. Stock (2004), Late Quaternary glaciation of the upper Soča River region (southern Julian Alps, NW Slovenia), *Sediment. Geol.*, *165*(3), 265–283.
- Bavec, M., M. Car, R. Stopar, P. Jamšek, and A. Gosar (2012), Geophysical evidence for the recent activity of the Idrija fault in Kanomlja, NW Slovenia, *RMZ Mater. Geoenviron.*, *59*, 247–256.
- Bavec, M., et al. (2013), Evidence of Idrija fault seismogenic activity during the late Holocene including the 1511  $M_m$  6.8 earthquake. *Proceedings: 4th International INQUA Meeting on Paleoseismology, Active Tectonics and Archeoseismology*.
- Benedetti, L., P. Tapponnier, G. C. King, B. Meyer, and I. Manighetti (2000), Growth folding and active thrusting in the Montello region, Veneto, northern Italy, *J. Geophys. Res.*, *105*(B1), 739–766, doi:10.1029/1999JB900222.
- Benedetti, L., I. Manighetti, Y. Gaudemer, R. Finkel, J. Malavieille, K. Pou, M. Arnold, G. Aumaitre, D. Bourlès, and K. Keddadouche (2013), Earthquake synchrony and clustering on Fucino faults (Central Italy) as revealed from in situ  $^{36}\text{Cl}$  exposure dating, *J. Geophys. Res. Solid Earth*, *118*, 4948–4974, doi:10.1002/jgrb.50299.
- Braucher, R., P. Del Castillo, L. Siame, A. J. Hidy, and D. L. Bourles (2009), Determination of both exposure time and denudation rate from an in situ-produced  $^{10}\text{Be}$  depth profile: A mathematical proof of uniqueness. Model sensitivity and applications to natural cases, *Quat. Geochronol.*, *4*(1), 56–67.
- Brückl, E., M. Behm, K. Decker, M. Grad, A. Guterch, G. R. Keller, and H. Thybo (2010), Crustal structure and active tectonics in the Eastern Alps, *Tectonics*, *29*, TC2011, doi:10.1029/2009TC002491.
- Bull, W. B. (2008), *Tectonic Geomorphology of Mountains: A New Approach to Paleoseismology*, John Wiley, Chichester, England.
- Buser, S. (1968), Osnovna geološka karta SFRJ, list Gorica, 1: 100 000 Zvezni geološki zavod, Beograd.
- Buser, S., K. Grad, and M. Pleničar (1967), Osnovna geološka karta SFRJ, list Postojna, 1:100.000. *Zvezni geološki zavod., Beograd*.
- Buser, S., B. Aničić, J. Cajhen, K. Ciglar, L. Ferjančič, B. Jurkovšek, I. Mlakar, D. Novak, R. Petrica, and M. Toman (1986), Osnovna geološka karta SFRJ, list Tolmin, 1:100.000. *Zvezni geološki zavod., Beograd*.
- Calais, E., J. M. Nocquet, F. Jouanne, and M. Tardy (2002), Current strain regime in the Western Alps from continuous Global Positioning System measurements, 1996–2001, *Geology*, *30*(7), 651–654.
- Calais, E., C. DeMets, and J. M. Nocquet (2003), Evidence for a post-3.16-Ma change in Nubia–Eurasia–North America plate motions?, *Earth Planet. Sci. Lett.*, *216*(1), 81–92.
- Camassi, R., C. H. Caracciolo, V. Castellani, and D. Slejko (2011), The 1511 eastern Alps earthquakes: A critical update and comparison of existing macroseismic datasets, *J. Seismol.*, *15*, 191–213.
- Caporali, A., et al. (2008), Geokinematics of Central Europe: New insights from the CERGOP-2/Environment Project, *J. Geodyn.*, *45*(4), 246–256.
- Caporali, A., F. Neubauer, L. Ostini, G. Stangl, and D. Zuliani (2013), Modeling surface GPS velocities in the Southern and Eastern Alps by finite dislocations at crustal depths, *Tectonophysics*, *590*, 136–150.

- Čar, J. (2010), Geološka zgradba idrijsko-cerkljanskega hribovja: Tolmač h Geološki karti idrijsko-cerkljanskega hribovja med Stopnikom in Rovtami v merilu 1: 25 000 = Geological structure of the Idrija-Cerkno hills Explanatory book to the Geological map of the Idrija-Cerkljansko hills between Stopnik and Rovte 1: 25 000. *Geological survey of Slovenija, Ljubljana*.
- Cheloni, D., N. D'Agostino, and G. Selvaggi (2014), Interseismic coupling, seismic potential, and earthquake recurrence on the southern front of the Eastern Alps (NE Italy). *J. Geophys. Res. Solid Earth*, *119*, 4448–4468, doi:10.1002/2014JB010954.
- Chiarialuze, L., et al. (2004), Complex normal faulting in the Apennines thrust-and-fold belt: The 1997 seismic sequence in central Italy. *Bull. Seismol. Soc. Am.*, *94*(1), 99–116.
- Csontos, L., A. Nagymarosy, F. Horváth, and M. Kovac (1992), Tertiary evolution of the Intra-Carpathian area: A model. *Tectonophysics*, *208*(1), 221–241.
- Cunningham, D., S. Grebbby, K. Tansey, A. Gosar, and V. Kastelic (2006), Application of airborne lidar to mapping seismogenic faults in forested mountainous terrain, southeastern Alps, Slovenia. *Geophys. Res. Lett.*, *33*, L20308, doi:10.1029/2006GL027014.
- D'Agostino, N., R. Giuliani, M. Mattone, and L. Bonci (2001), Active crustal extension in the central Apennines (Italy) inferred from GPS measurements in the interval 1994–1999. *Geophys. Res. Lett.*, *28*(10), 2121–2124, doi:10.1029/2000GL012462.
- D'Agostino, N., D. Cheloni, S. Mantenuto, G. Selvaggi, A. Michelini, and D. Zuliani (2005), Strain accumulation in the Southern Alps (NE Italy) and deformation at the northeastern boundary of Adria observed by CGPS measurements. *Geophys. Res. Lett.*, *32*, L19306, doi:10.1029/2005GL024266.
- D'Agostino, N., A. Avallone, D. Cheloni, E. D'Anastasio, S. Mantenuto, and G. Selvaggi (2008), Active tectonics of the Adriatic region from GPS and earthquake slip vectors. *J. Geophys. Res.*, *113*, B12413, doi:10.1029/2008JB005860.
- Davis, K., D. W. Burbank, D. Fisher, S. Wallace, and D. Nobes (2005), Thrust-fault growth and segment linkage in the active Ostler fault zone, New Zealand. *J. Struct. Geol.*, *27*(8), 1528–1546.
- Delunel, R., P. A. Beek, D. L. Bourlès, J. Carcaillet, and F. Schlunegger (2014), Transient sediment supply in a high-altitude Alpine environment evidenced through a <sup>10</sup>Be budget of the Etages catchment (French Western Alps). *Earth Surf. Processes Landforms*, *39*(7), 890–899.
- Fifield, L. K., T. R. Ophel, G. L. Allan, J. R. Bird, and R. F. Davie (1990), Accelerator mass spectrometry at the Australian National University's 14UD accelerator: Experience and developments. *Nucl. Instrum. Methods Phys. Res. Sect. B*, *52*(3), 233–237.
- Fitzko, F., P. Suhadolc, A. Aoudia, and G. F. Panza (2005), Constraints on the location and mechanism of the 1511 Western-Slovenia earthquake from active tectonics and modeling of macroseismic data. *Tectonophysics*, *404*(1), 77–90.
- Fontana, A., P. Mozzi, and A. Bondesan (2008), Alluvial megafans in the Veneto-Friuli Plain: Evidence of aggrading and erosive phases during late Pleistocene and Holocene. *Quat. Int.*, *189*(7).
- Galadini, F. (1999), Pleistocene changes in the central Apennine fault kinematics: A key to decipher active tectonics in central Italy. *Tectonics*, *18*(5), 877–894, doi:10.1029/1999TC900020.
- Gosse, J. C., and F. M. Phillips (2001), Terrestrial in situ cosmogenic nuclides: Theory and application. *Quat. Sci. Rev.*, *20*(14), 1475–1560.
- Grenerczy, G., G. Sella, S. Stein, and A. Kenyeres (2005), Tectonic implications of the GPS velocity field in the northern Adriatic region. *Geophys. Res. Lett.*, *32*, L16311, doi:10.1029/2005GL022947.
- Habič, P. (1968), Kraški svet med Idrijco in Vipavo-The karstic region between the Idrija and Vipava rivers. *Dela-Opera SAZU*, *21*, 243pp.
- Habič, P. (1997), Karst hydrogeological investigations in south-western Slovenia. *Acta Carsol.*, *29*, 1.
- Herak, M., D. Herak, and S. Markušić (1995), Fault plane solutions for earthquakes (1956–1995) in Croatia and neighboring regions. *Geofizika*, *12*(1), 43–56.
- Hetzl, R., and A. Hampel (2005), Slip rate variations on normal faults during glacial–interglacial changes in surface loads. *Nature*, *435*(7038), 81–84.
- Hippolyte, J. C., J. Angelier, and F. B. Roure (1994), A major geodynamic change revealed by Quaternary stress patterns in the southern Apennines (Italy). *Tectonophysics*, *230*(3), 199–210.
- Horváth, F. (1995), Phases of compression during the evolution of the Pannonian Basin and its bearing on hydrocarbon exploration. *Mar. Pet. Geol.*, *12*(8), 837–844.
- Hubert-Ferrari, A., Armijo, R., King, G., Meyer, B., and Barka, A. (2002), Morphology, displacement, and slip rates along the North Anatolian Fault, Turkey. *J. Geophys. Res.*, *107*(B10), 2235, doi:10.1029/2001JB000393.
- Jamšek Rupnik, P., L. Benedetti, M. Bavec, and M. Vrabec (2012), Geomorphic indicators of Quaternary activity of the Sava fault between Golnik and Preddvor. *RMZ – Mater. Geovviron.*, *59*(2/3), 299–314.
- Jamšek-Rupnik, P. (2013), Geomorphological evidence of active tectonics in the Ljubljana Basin: Doctoral dissertation (Doctoral dissertation, P. Jamšek Rupnik).
- Kastelic, V., M. Vrabec, D. Cunningham, and A. Gosar (2008), Neo-Alpine structural evolution and present-day tectonic activity of the eastern Southern Alps: The case of the Ravne Fault, NW Slovenia. *J. Struct. Geol.*, *30*(8), 963–975.
- Lavé, J., and J. P. Avouac (2000), Active folding of fluvial terraces across the Siwaliks Hills, Himalayas of central Nepal. *J. Geophys. Res.*, *105*(B3), 5735–5770, doi:10.1029/1999JB900292.
- Lisiecki, L. E., and M. E. Raymo (2005), A Pliocene-Pleistocene stack of 57 globally distributed benthic  $\delta^{18}\text{O}$  records. *Paleoceanography*, *20*, PA1003, doi:10.1029/2004PA001071.
- Manighetti, I., G. C. P. King, Y. Gaudemer, C. H. Scholz, and C. Doubre (2001), Slip accumulation and lateral propagation of active normal faults in Afar. *J. Geophys. Res.*, *106*(B7), 13,667–13,696, doi:10.1029/2000JB900471.
- Manighetti, I., M. Campillo, C. Sammis, P. M. Mai, and G. King (2005), Evidence for self-similar, triangular slip distributions on earthquakes: Implications for earthquake and fault mechanics. *J. Geophys. Res.*, *110*, B05302, doi:10.1029/2004JB003174.
- Márton, E., L. Fodor, B. Jelen, P. Márton, H. Rífelj, and R. Kevrić (2002), Miocene to Quaternary deformation in NE Slovenia: Complex paleomagnetic and structural study. *J. Geodyn.*, *34*(5), 627–651.
- Márton, E., K. Drobne, V. Čosović, and A. Moro (2003), Palaeomagnetic evidence for Tertiary counterclockwise rotation of Adria. *Tectonophysics*, *377*(1), 143–156.
- Mattei, M., F. Cifelli, and N. D'Agostino (2007), The evolution of the Calabrian Arc: Evidence from paleomagnetic and GPS observations. *Earth Planet. Sci. Lett.*, *263*(3), 259–274.
- McKenzie, D. (1972), Active tectonics of the Mediterranean region. *Geophys. J. Int.*, *30*(2), 109–185.
- Merritts, D. J., K. R. Vincent, and E. E. Wohl (1994), Long river profiles, tectonism, and eustasy: A guide to interpreting fluvial terraces. *J. Geophys. Res.*, *99*(B7), 14,031–14,050, doi:10.1029/94JB00857.
- Miller, K. G., et al. (2005), The Phanerozoic record of global sea-level change. *Science*, *310*(5752), 1293–1298.
- Monegato, G., C. Ravazzi, M. Donegana, R. Pini, G. Calderoni, and L. Wick (2007), Evidence of a two-fold glacial advance during the last glacial maximum in the Tagliamento end moraine system (eastern Alps). *Quat. Res.*, *68*(2), 284–302.
- Moulin, A., L. Benedetti, A. Gosar, P. J. Rupnik, M. Rizza, D. Bourlès, and J. F. Ritz (2014), Determining the present-day kinematics of the Idrija fault (Slovenia) from airborne lidar topography. *Tectonophysics*, *628*, 188–205.

- Nicol, A., J. Walsh, K. Berryman, and S. Nodder (2005), Growth of a normal fault by the accumulation of slip over millions of years, *J. Struct. Geol.*, *27*(2), 327–342.
- Nicol, A., J. Walsh, V. Mouslopoulou, and P. Villamor (2009), Earthquake histories and Holocene acceleration of fault displacement rates, *Geology*, *37*(10), 911–914.
- Nocquet, J. M. (2012), Present-day kinematics of the Mediterranean: A comprehensive overview of GPS results, *Tectonophysics*, *579*, 220–242.
- Nocquet, J. M., and E. Calais (2004), Geodetic measurements of crustal deformation in the Western Mediterranean and Europe, *Pure Appl. Geophys.*, *161*(3), 661–681.
- Oldow, J. S., L. Ferranti, D. S. Lewis, J. K. Campbell, B. d'Argenio, R. Catalano, G. Pappone, L. Carmignani, P. Conti, and C. L. V. Aiken (2002), Active fragmentation of Adria, the North African promontory, central Mediterranean orogen, *Geology*, *30*(9), 779–782.
- Paiero, G., and G. Monegato (2003), The Pleistocene evolution of Arzino alluvial fan and western part of Tagliamento morainic amphitheatre (Friuli, NE Italy), *Il Quat.*, *16*(1), 185–193.
- Peltzer, G., P. Tapponnier, Y. Gaudemer, B. Meyer, S. Guo, K. Yin, and H. Dai (1988), Offsets of late Quaternary morphology, rate of slip, and recurrence of large earthquakes on the Chang Ma fault (Gansu, China), *J. Geophys. Res.*, *93*(B7), 7793–7812, doi:10.1029/JB093iB07p07793.
- Peresson, H., and K. Decker (1997), Far-field effects of Late Miocene subduction in the Eastern Carpathians: E-W compression and inversion of structures in the Alpine-Carpathian-Pannonian region, *Tectonics*, *16*(1), 38–56, doi:10.1029/96TC02730.
- Piccardi, L., Y. Gaudemer, P. Tapponnier, and M. Boccaletti (1999), Active oblique extension in the central Apennines (Italy): Evidence from the Fucino region, *Geophys. J. Int.*, *139*(2), 499–530.
- Picha, F. J. (2002), Late orogenic strike-slip faulting and escape tectonics in frontal Dinarides-Hellenides, Croatia, Yugoslavia, Albania, and Greece, *AAPG Bull.*, *86*(9), 1659–1671.
- Placer, L., M. Vrabec, and B. Celarc (2010), The bases for understanding of the NW Dinarides and Istria Peninsula tectonics, *Geologija*, *53*(1), 55–86.
- Poljak, M., M. Živčić, and P. Zupančič (2000), *The Seismotectonic Characteristics of Slovenia*, pp. 37–55, Birkhäuser, Basel, Switzerland.
- Poljak, M., A. Gosar, and M. Živčić (2010), Active tectonics in Slovenia, *GeoActa, Spec. Publ.*, *3*, 15–24.
- Pondrelli, S., S. Salimbeni, G. Ekström, A. Morelli, P. Gasperini, and G. Vannucci (2006), The Italian CMT dataset from 1977 to the present, *Phys. Earth Planet. Inter.*, *159*(3), 286–303.
- Ratschbacher, L., W. Frisch, H. G. Linzer, and O. Merle (1991), Lateral extrusion in the Eastern Alps, part 2: Structural analysis, *Tectonics*, *10*(2), 257–271, doi:10.1029/90TC02623.
- Replumaz, A., R. Lacassin, P. Tapponnier, and P. H. Leloup (2001), Large river offsets and Plio-Quaternary dextral slip rate on the Red River fault (Yunnan, China), *J. Geophys. Res.*, *106*(B1), 819–836, doi:10.1029/2000JB900135.
- Ribarič, V. (1979), The Idrija earthquake of March 26, 1511—A reconstruction of some seismological parameters, *Tectonophysics*, *53*(3), 315–324.
- Rockwell, T. K., and Y. Klinger (2013), Surface rupture and slip distribution of the 1940 Imperial Valley earthquake, Imperial Fault, Southern California: Implications for rupture segmentation and dynamics, *Bull. Seismol. Soc. Am.*, *103*(2A), 629–640.
- Rockwell, T. K., S. Lindvall, M. Herzberg, D. Murbach, T. Dawson, and G. Berger (2000), Paleoseismology of the Johnson Valley, Kickapoo, and Homestead Valley faults: Clustering of earthquakes in the eastern California shear zone, *Bull. Seismol. Soc. Am.*, *90*(5), 1200–1236.
- Royden, L. H. (1993), Evolution of retreating subduction boundaries formed during continental collision, *Tectonics*, *12*(3), 629–638, doi:10.1029/92TC02641.
- Ryb, U., A. Matmon, Y. Erel, I. Haviv, A. Katz, A. Starinsky, A. Angert, and A. Team (2014), Controls on denudation rates in tectonically stable Mediterranean carbonate terrain, *Geol. Soc. Am. Bull.*, *126*(3–4), 553–568.
- Sadier, B., J. J. Delannoy, L. Benedetti, D. L. Bourlès, S. Jaillet, J. M. Geneste, A.-E. Lebatard, and M. Arnold (2012), Further constraints on the Chauvet cave artwork elaboration, *Proc. Natl. Acad. Sci. U.S.A.*, *109*(21), 8002–8006.
- Saillard, M., C. Petit, Y. Rolland, R. Braucher, D. L. Bourlès, S. Zerathe, M. Revel, and A. Jourdon (2014), Late Quaternary incision rates in the Vésubie catchment area (Southern French Alps) from in situ-produced <sup>36</sup>Cl cosmogenic nuclide dating: Tectonic and climatic implications, *J. Geophys. Res. Earth Surf.*, *119*, 1121–1135, doi:10.1002/2013JF002985.
- Schattner, U. (2010), What triggered the early-to-mid Pleistocene tectonic transition across the entire eastern Mediterranean?, *Earth Planet. Sci. Lett.*, *289*(3), 539–548.
- Schimmelpfennig, I., L. Benedetti, R. Finkel, P. H. Blard, D. Bourlès, P. Burnard, and A. Williams (2009), Sources of in-situ <sup>36</sup>Cl in basaltic rocks. Implications for calibration of production rates, *Quat. Geochronol.*, *4*(6), 441–461.
- Schimmelpfennig, I., L. Benedetti, V. Garreta, R. Finkel, P. H. Blard, P. Burnard, D. Bourlès, R. Finkel, K. Ammon, and T. Dunai (2011), Calibration of cosmogenic <sup>36</sup>Cl production rates from Ca and K spallation in lava flows from Mt. Etna (38°N, Italy) and Payun Matru (36°S, Argentina), *Geochim. Cosmochim. Acta*, *75*(10), 2611–2632.
- Schlagenhauf, A., I. Manighetti, L. Benedetti, Y. Gaudemer, R. Finkel, J. Malavieille, and K. Pou (2011), Earthquake supercycles in Central Italy, inferred from <sup>36</sup>Cl exposure dating, *Earth Planet. Sci. Lett.*, *307*(3), 487–500.
- Scholz, C. H. (2002), *The Mechanics of Earthquakes and Faulting*, Cambridge Univ. Press, Cambridge, U. K.
- Scholz, C. H. (2010), Large earthquake triggering, clustering, and the synchronization of faults, *Bull. Seismol. Soc. Am.*, *100*(3), 901–909.
- Sharma, P., P. W. Kubik, U. Fehn, H. E. Gove, K. Nishiizumi, and D. Elmore (1990), Development of <sup>36</sup>Cl standards for AMS, *Nucl. Instrum. Methods Phys. Res. Sect. B*, *52*(3), 410–415.
- Siame, L., et al. (2004), Local erosion rates versus active tectonics: Cosmic ray exposure modeling in Provence (south-east France), *Earth Planet. Sci. Lett.*, *220*(3), 345–364.
- Stone, J. O. (2000), Air pressure and cosmogenic isotope production, *J. Geophys. Res.*, *105*(B10), 23,753–23,759, doi:10.1029/2000JB900181.
- Stone, J. O., G. L. Allan, L. K. Fifield, and R. G. Cresswell (1996), Cosmogenic chlorine-36 from calcium spallation, *Geochim. Cosmochim. Acta*, *60*(4), 679–692.
- Šumanovac, F., J. Orešković, and M. Grad (2009), Crustal structure at the contact of the Dinarides and Pannonian basin based on 2-D seismic and gravity interpretation of the Alp07 profile in the ALP 2002 experiment, *Geophys. J. Int.*, *179*(1), 615–633.
- Tomljenović, B., and L. Csontos (2001), Neogene–Quaternary structures in the border zone between Alps, Dinarides and Pannonian Basin (Hrvatsko zagorje and Karlovac Basins, Croatia), *Int. J. Earth Sci.*, *90*(3), 560–578.
- Vaia, F. (1982), Depositi proglaciali nella pedemontana friulana, *Incontri*, *1*, 2–10.
- Vrabec, M., and L. Fodor (2006), Late Cenozoic tectonics of Slovenia: Structural styles at the northeastern corner of the Adriatic microplate, in *The Adria Microplate: GPS Geodesy, Tectonics and Hazards*, pp. 151–168, Springer, Netherlands.
- Vrabec, M., P. P. Preseren, and B. Stopar (2006), GPS study (1996–2002) of active deformation along the Periadriatic fault system in north-eastern Slovenia: Tectonic model, *Geol. Carpathica-Bratislava*, *57*(1), 57.
- Ward, S. N. (1994), Constraints on the seismotectonics of the central Mediterranean from very long baseline interferometry, *Geophys. J. Int.*, *117*(2), 441–452.

- Weber, J., M. Vrabec, P. Pavlovčič-Prešeren, T. Dixon, Y. Jiang, and B. Stopar (2010), GPS-derived motion of the Adriatic microplate from Istria Peninsula and Po Plain sites, and geodynamic implications, *Tectonophysics*, *483*(3), 214–222.
- Westaway, R. (1990), Present-day kinematics of the plate boundary zone between Africa and Europe, from the Azores to the Aegean, *Earth Planet. Sci. Lett.*, *96*(3), 393–406.
- Winter, T., J. P. Avouac, and A. Lavenu (1993), Late Quaternary kinematics of the Pallatanga strike-slip fault (Central Ecuador) from topographic measurements of displaced morphological features, *Geophys. J. Int.*, *115*(3), 905–920.
- Žibret, L. (2015), Kinematic and paleostress evolution of the NW-SE trending Dinaric faults in the northwestern external Dinarides: Doctoral dissertation (Doctoral dissertation, L. Žibret).